Nuanced role for dendritic cell intrinsic IRE1 RNase in the regulation of antitumor adaptive immunity

Felipe Flores-Santibañez[1,8,9], Sofie Rennen[2,3,9], Dominique Fernandez[1], Clint De Nolf[2], Sandra Gaete[1], Camila Fuentes[4], Carolina Moreno[1], Diego Figueroa[5], Álvaro Lladser[5,6], Takao Iwawaki[7], María Rosa Bono[8], Sophie Janssens[2,3,*] and Fabiola Osorio[1,*]

[1]Laboratory of Immunology and Cellular Stress, Immunology Program, Institute of Biomedical Sciences, Faculty of Medicine, University of Chile, Av. Independencia 1027, 8380453, Santiago, Chile.
[2]Laboratory for ER Stress and Inflammation, VIB Center for Inflammation Research, Technologiepark, Zwijnaarde 71, B-9052, Ghent, Belgium.
[3]Department of Internal Medicine and Pediatrics, Ghent University, De Pintelaan 185, 9000, Ghent, Belgium.
[4]Laboratory of Cancer Immunoregulation, Immunology Program, Institute of Biomedical Sciences, Faculty of Medicine, University of Chile, Av. Independencia 1027, 8380453, Santiago, Chile.
[5]Laboratory of Immunoncology, Fundación Ciencia & Vida, Av Zañartu 1482, 7780272, Santiago, Chile.
[6]Faculty of Medicine and Science, Universidad San Sebastián, Lota 2465, 7510157 Santiago, Chile.
[7]Division of Cell Medicine, Department of Life Science, Medical Research Institute, Kanazawa Medical University, 1-1 Daigaku, Uchinada, Kahoku, Ishikawa 920-0293 Ishikawa, Japan.
[8]Immunology Laboratory, Biology Department, Faculty of Sciences, University of Chile, Las Palmeras 3425, 7800003, Santiago, Chile.
[9] These authors equally contributed to this work.
* Corresponding authors.

Running title: Nuanced role for DC-intrinsic IRE1 RNase in antitumor immunity

Conflict of interest statement: "The authors have declared that no conflict of interest exists."

Correspondence: Fabiola Osorio
Immunology Program
Institute of Biomedical Sciences
Faculty of Medicine
Universidad de Chile
Av. Independencia 1027
Postal code: 8380453
Santiago
Chile
Phone: +56-2-29789503
Email: fabiolaosorio@med.uchile.cl

Sophie Janssens
Laboratory for Endoplasmic Reticulum Stress and Inflammation
VIB Center for Inflammation Research,
Technologiepark 71
B-9052 Zwijnaarde
Ghent
Belgium
Email: sophie.janssens@irc.vib-ugent.be

ABSTRACT

The IRE1/XBP1s axis of the unfolded protein response (UPR) plays divergent roles in dendritic cell (DC) biology in steady state versus tumor contexts. Whereas tumor associated DCs show dysfunctional IRE1/XBP1s activation that curtails their function, the homeostasis of conventional type 1 DCs (cDC1) in tissues requires intact IRE1 RNase activity. Considering that cDC1s are key orchestrators of antitumor immunity, it is relevant to understand the functional versus dysfunctional roles of IRE1/XBP1s in tumor DC subtypes. Here, we show that cDC1s constitutively activate IRE1 RNase within subcutaneous B16 melanoma and MC38 adenocarcinoma tumor models. Mice lacking XBP1s in DCs display increased melanoma tumor growth, reduced T cell effector responses and accumulation of terminal exhausted $CD8^+$ T cells. Transcriptomic studies revealed that XBP1 deficiency in tumor cDC1s decreased expression of mRNAs encoding XBP1s and regulated IRE1 dependent decay (RIDD) targets. Finally, we find that the dysregulated melanoma growth and impaired T cell immunity noticed in XBP1 deficient mice are attributed to RIDD induction in DCs. This work indicates that IRE1 RNase activity in melanoma/MC38-associated DCs fine tunes aspects of antitumor immunity independently of XBP1s, revealing a differential role for the UPR axis that depends on the DC subtype and cancer model.

Keywords: Dendritic cells, immunity, IRE1, melanoma, unfolded protein response.

107 **ABBREVIATIONS**

108

109 BM: bone marrow

110 cDC: conventional DC

111 cDC1: type 1conventional DC ($XCR1^+$ DC)

112 cDC2: type 2conventional DC ($CD11b^+$ DC)

113 DC: dendritic cell

114 DEG: Differentially expressed gene

115 ER: endoplasmic reticulum

116 ERAI: ER stress-activated indicator

117 Flt3L: FMS-related tyrosine kinase 3 ligand

118 FP: fluorescent protein

119 GSEA: Gene set enrichment analysis

120 IRE1: inositol-requiring enzyme 1 alpha

121 KO: Knock-out

122 MdC: Myeloid derived Cell

123 RIDD: regulated IRE1-dependent decay

124 ROS: reactive oxygen species

125 TAM: tumor-associated macrophages

126 TCR: T cell receptor

127 TdLN: Tumor draining lymph node

128 UPR: unfolded protein response

129 XBP1s: spliced XBP1

130 XBP1u: unspliced XBP1

131

132

133

134

135

136

137 # INTRODUCTION

138 A crucial arm of antitumor immunity relies on effective activation of tumor specific
139 cytotoxic CD8$^+$ T cells endowed with the ability to eliminate cancer cells. This process is
140 critically dependent on type 1 conventional dendritic cells (cDC1), which excel in cross-
141 presentation of tumor-associated antigens (1–3), secrete soluble factors that potentiate
142 CD8$^+$ T cell function (2, 4–7), and prevent the generation of terminal exhausted CD8$^+$ T
143 cells committed to irreversible dysfunctional phenotypes in tumors (8). Tumor cDC1
144 infiltration correlates with improved prognosis (2, 5, 9) and better response to immune
145 checkpoint blockade (ICB) therapy (9–12). Besides, therapeutic strategies
146 expanding/activating tumor cDC1s have shown promising results in clinical trials (11, 13,
147 14). Additional DC subsets such as type 2 DCs (cDC2s), and a novel DC activation state
148 termed 'mregDCs' (mature DCs enriched in immunoregulatory molecules) can also boost
149 antitumor CD4$^+$ and CD8$^+$ T cell responses (7, 15–17), indicating that cDCs are interesting
150 candidates in immunotherapy. However, the molecular mechanisms safeguarding the
151 function of these cells in tumors have not been fully elucidated.

152 An emerging intracellular pathway regulating DC biology is the inositol-requiring enzyme
153 1 alpha (IRE1) branch of the unfolded protein response (UPR), which is an adaptive
154 cellular response maintaining the fidelity of the cellular proteome (18). Upon
155 endoplasmic reticulum (ER) stress, the endoribonuclease (RNase) domain of IRE1 splices
156 *Xbp1* mRNA, generating the transcription factor XBP1 spliced (XBP1s), master regulator
157 of protein folding and ER biogenesis (18–20). The IRE1 RNase domain can also promote
158 the degradation of a subset of mRNAs/miRNAs in a process known as 'regulated IRE1-
159 dependent decay' (RIDD) (21), which is a mechanism beginning to be understood in
160 pathological settings including metabolism, inflammation and cancer (22–24).

161 In steady state, IRE1 regulates cDC homeostasis via constitutive activation of its RNase
162 domain, a feature noticed in cDC1s across several tissues (25, 26). Furthermore, cDC1s
163 are markedly sensitive to perturbations in the IRE1/XBP1s axis, as genetic loss of the
164 transcription factor XBP1 alters proteostatic programs and counter activates the RIDD
165 branch, which mediates the decay of various mRNAs involved in integrin expression, ER
166 to golgi transport and antigen presentation, among others (25, 26). The selectivity of the
167 IRE1/XBP1s axis in cDC1s is underscored in microarray studies of XBP1 deficient cells,
168 which change the transcriptomic landscape of cDC1s but not cDC2s (26). As such, cDC1s
169 opt the IRE1/XBP1s axis for proper function in steady state, but it is unclear if the pathway
170 displays similar roles in cDC1s infiltrating tumors. This is a relevant question, as reported
171 work shows that metabolically stressed tumors elicit maladaptive UPR activation in
172 certain tumor immune cells (including DCs), which reprograms their phenotype towards
173 dysfunctional states that promote tumor growth (27, 28). For instance, DCs infiltrating
174 ovarian cancer (typified by expression of the cDC2/monocyte marker CD11b^{+} (29))
175 display persistent IRE1/XBP1s activation that triggers aberrant intracellular lipid
176 accumulation, resulting in impaired immunostimulatory functions and leading to tumor
177 progression (30). Thus, these data suggest that IRE1 may play different, or even opposite
178 roles in DC biology depending on the subtype or the inflammatory context. As such, a
179 correct delineation of the role of the enzyme in tumor cDCs is required to understand if
180 intervention of this UPR branch can be targeted for potential cancer therapies.
181 In this work, we study the role of IRE1/XBP1s in DCs by focusing on two
182 immunoresponsive tumor models: subcutaneous mouse B16/B78 melanoma and MC38
183 colon adenocarcinoma (2, 10). We identified that cDC1s display constitutive IRE1 RNase
184 activity in tumors, which follows a lineage-intrinsic trait not influenced by the tumor
185 microenvironment. In contrast to previous reports (30), deletion of XBP1 in DCs did not

186 decrease tumor burden. Rather, XBP1 deficiency in DCs resulted in a moderate increase
187 of tumor growth, lower frequencies of intratumoral effector T cells, and accumulation of
188 terminal exhausted TIM-3^{+}CD8^{+} cells in the melanoma model. Transcriptomic studies
189 revealed that XBP1 deficient tumor cDC1s downregulate proteostatic processes and
190 decrease the expression of mRNAs encoding XBP1s and regulated IRE1 dependent decay
191 (RIDD) targets. Importantly, animals bearing double deletion of IRE1 RNase and XBP1 in
192 DCs display normal tumor growth and adaptive immunity in the melanoma model,
193 highlighting a role for IRE1 RNase hyperactivation in fine tuning aspects of antitumor
194 immunity via DCs.
195
196
197
198
199
200
201
202
203
204
205
206
207
208
209
210

211 # RESULTS

212 **cDC1s constitutively activate IRE1 RNase in subcutaneous melanoma and MC38**
213 **colon carcinoma tumors**

214 The tumor microenvironment contain activators of the IRE1/XBP1s axis that are detected
215 by immune cells (27, 30–32). To identify relevant cell types activating IRE1 RNase in
216 tumors, we analyzed the immune composition of B16 tumors of ERAI mice, a mouse strain
217 that reports IRE1 RNase activity through expression of Venus Fluorescent Protein
218 (VenusFP) fused with the sequence of *Xbp1s* mRNA (33) (validated in (25, 26, 31)). To
219 allow unsupervised identification of IRE1 RNase cellular targets, we devised a 17-color
220 flow cytometry panel and data was visualized on a *t*-distributed stochastic neighbor
221 embedding (*t*-SNE) map. Cells were grouped into populations by DBScan-guided
222 automated clustering (Fig. 1A-B, Supp. Fig. 1A), which identified 15 cell clusters that
223 included $CD8^+$ T cells, $CD4^+$ T cells, monocyte-derived cells (MdCs), MHC-II-expressing
224 MdCs, NK cells, NKT cells, B cells, neutrophils and cDC1s. As expected (17), cDC2s and
225 tumor associated macrophages (TAMs) (clusters 4 and 6) showed a degree of
226 heterogeneity and convergence. Also, our analysis revealed two undefined clusters based
227 on surface marker expression; Cluster 11: $CD4^+$ $CD11c^+$ $CD26^+$, and Cluster 14: $CD3^+$ $CD4^+$
228 $CD11b^{int}$ $F4/80^+$ MHC-II^{high} $CD11c^{int}$ $CD26^{high}$.

229 Next, IRE1 RNase activity from the ERAI reporter mice line was determined in the clusters
230 of the t-SNE plot (Fig. 1C-D). Data indicated that among $CD45^+$ hematopoietic cells, cDC1s
231 represented the population with highest fluorescence intensity of VenusFP (Fig 1C-D,
232 cluster 15). Additional immune cells including cDC2s, MdC, MHC-II^+MdC, TAM,
233 neutrophils, NK cells and cells from cluster 11 also showed noticeable VenusFP induction,
234 albeit at lower levels than cDC1s; whereas $CD4^+$ T cells, $CD8^+$ T cells and B cells showed
235 little or no induction of VenusFP compared to cells from control animals (Fig 1D). Manual

236 gating analysis (Fig. 1E-F, Supp. Fig. 2A) confirmed that the mean fluorescence intensity
237 (MFI) of VenusFP in melanoma-associated cDC1s was higher than additional myeloid and
238 lymphoid cells (Fig. 1E-F). Notably, similar results were observed in cDC1s infiltrating
239 MC38 tumors (Supp. Fig. 1B). Finally, these data was confirmed by PCR for endogenous
240 *Xbp1* spliced and unspliced forms from tumor cDC1s isolated from wild type (WT)
241 animals implanted with the B16-FLT3L melanoma cell line (which expresses the DC-
242 differentiation factor FMS-like tyrosine kinase 3 ligand (FLT3L) (11, 34)). Data in Fig. 1G-
243 H showed that tumor cDC1s expressed marked levels of *Xbp1s*, which was even superior
244 to the levels noticed in bone-marrow derived DCs (BMDC) stimulated with the
245 pharmacological UPR inducer tunicamycin. Altogether, these data indicate that cDC1s
246 display prominent activation of the IRE1/XBP1s axis in tumors.
247 We next interrogated whether the augmented IRE1 RNase activity observed in tumor
248 cDC1s is a lineage-intrinsic signature or if it is a feature imposed by the tumor
249 microenvironment. We quantified the VenusFP MFI of cDC1s directly exposed to the
250 tumor (tumor cDC1 and migratory cDC1s of the tumor draining lymph node (TdLN)),
251 versus TdLN resident cDC1s, which do not access to the tumor site (gating strategy in
252 Supp. Fig. 2B) (35). Data depicted in Fig. 1I indicates that tumor cDC1s express lower
253 levels of VenusFP than resident cDC1s, indicating that tumor exposure does not increase
254 IRE1 RNase activity in these cells. Similar observations were made for cDC2s (Fig 1I). In
255 fact, cDC1s infiltrating MC38 tumors express markedly lower levels of VenusFP than
256 spleen cDC1s (Supp. Fig. 1C). Of note, this observation was not replicated in monocytes,
257 which express higher VenusFP levels in the tumor compared to the spleen (Fig 1J).
258 Altogether, these data suggest that IRE1 RNase activation in tumor cDCs is a stable lineage
259 intrinsic trait not driven by the microenvironment.
260

261 **XBP1 deletion in CD11c-expressing cells results in increased melanoma tumor**
262 **growth**

263 To gain insights on the role of XBP1 in DCs during melanoma tumor growth, we studied
264 the *Itgax*-Cre x *Xbp1*$^{fl/fl}$ mice (36, 37), referred to as 'XBP1$^{\Delta DC}$' mice, in which exon 2 of
265 *Xbp1* is excised in CD11c-expressing cells, resulting in absence of the transcription factor
266 in DCs (26). These animals were compared to control littermates (*Xbp1*$^{fl/fl}$ animals with
267 no expression of Cre), referred to as 'XBP1^{WT}' mice. XBP1^{WT} and XBP1$^{\Delta DC}$ mice were
268 implanted with the B78-ChOVA melanoma line, a B16 variant that expresses the
269 ovalbumin (OVA) antigen and mCherry fluorescent protein (2). Data in Figure 2A-B
270 indicate that XBP1$^{\Delta DC}$ mice showed moderate but noticeable acceleration of tumor growth
271 and significantly larger tumor size than tumors from XBP1^{WT} mice on day 12 post
272 implantation (80.44 ± 8.927 vs 56.56 ± 6.174 mm^3, p = 0.0312, mean ± s.e.m.) (Fig. 2B).
273 As a second tumor model, we also analyzed growth of subcutaneous MC38 murine colon
274 adenocarcinoma tumors, which also showed a trend towards increased tumor growth in
275 XBP1$^{\Delta DC}$ mice, but without reaching statistical significance (Supp. Fig. 3A-C).

276 To understand if XBP1 deficiency in the CD11c compartment resulted in altered cell
277 recruitment, we quantified the immune cell composition at the melanoma tumor site.
278 XBP1^{WT} and XBP1$^{\Delta DC}$ mice show similar numbers of CD45$^+$ cells (Fig. 2C), and comparable
279 composition of tumor cDC1/cDC2 and resident and migratory cDC1/cDC2s in the TdLN
280 (Fig. 2D-E). Furthermore, conditional *knock-out* and control animals also showed
281 comparable frequencies of myeloid and lymphoid cells (Fig. 2F-H). These data indicate
282 that XBP1s expression by DCs infiltrating melanoma and MC38 tumor does not promote
283 tumor progression. Rather, loss of XBP1s in DCs leads to increased melanoma tumor
284 growth by mechanisms that are independent of immune cell recruitment.
285

286 **XBP1 deletion in CD11c-expressing cells results in impaired antitumor T cell**
287 **responses and disbalanced precursor/terminal exhausted T cell ratio**

288 We next focused our analysis on DC function. It was recently identified a conserved
289 immunoregulatory transcriptional program activated by tumor DCs based on the co-
290 expression of the molecules CD40 and PDL-1 plus the cytokine IL-12 (15). Our analysis
291 revealed that tumor and migratory cDC1/cDC2s from XBP1$^{\Delta DC}$ mice express normal levels
292 of these molecules (Fig. 3A, Supp. Fig. 4A). We also studied bone marrow cDC1s generated
293 upon culture with OP9-DL1 stromal cell line plus FLT3L (reported in (38, 39)). We found
294 that bone marrow cDC1s from XBP1$^{\Delta DC}$ mice produce lower levels of IL-12 in
295 unstimulated conditions (Fig 3B, Supp. Fig. 4B). However, upon tumor exposure,
296 expression of IL-12 was comparable between XBP1 sufficient and deficient cDC1s. We
297 conclude that XBP1s regulate certain parameters of DC activation in steady state that are
298 restored upon tumor encounter.

299 Considering previous findings showing that XBP1s deficient cDC1s have impaired cross-
300 presentation abilities in steady state (26), we interrogated if the mice line was able to
301 cross-present melanoma-associated antigens. We implanted B78ChOVA tumors in
302 XBP1^{WT} and XBP1$^{\Delta DC}$ mice and quantified the presence of endogenous OVA-specific CD8^{+}
303 T cells using H-2K^{b}-OVA$_{257-264}$ tetramers. XBP1^{WT} and XBP1$^{\Delta DC}$ contained similar
304 frequencies of OVA-specific CD8^{+} T cells in tumors and TdLN (Fig. 3C-D, Supp. Fig 4C). A
305 similar response was obtained when tracking proliferation/early activation of CD8^{+} T
306 cells isolated from pmel mice, which possess transgenic CD8^{+} T cells bearing a TCR
307 selective for the melanoma-associated antigen gp100 (40) (Supp. Fig. 4D-E). Thus, we
308 conclude that XBP1 deletion in tumor-associated CD11c^{+} cells does not prevent cross-
309 presentation of melanoma-associated antigens.

310 We next investigated the quality of the antitumor T cell response evoked in XBP1$^{\Delta DC}$ mice.
311 As a measure of T cell quality, we analyzed cytokine producing T cells from tumors of
312 XBP1^{WT} and XBP1$^{\Delta DC}$ mice. Tumors from XBP1$^{\Delta DC}$ mice contained lower frequencies of
313 IFN-γ-producing and TNF-producing CD8$^+$ T cells, which also resulted in decreased
314 frequencies of double producers IFN-γ$^+$TNF$^+$ CD8$^+$ T cells and triple producers IFN-
315 γ$^+$TNF$^+$IL-2$^+$ CD8$^+$ T cells (Fig. 3E-F). These observations were also noticed in the CD4$^+$ T
316 cell compartment, as reduced frequencies of IFN-γ$^+$ CD4$^+$ T cells and IFN-γ$^+$ TNF$^+$ CD4$^+$ T
317 cells were found in tumors from XBP1$^{\Delta DC}$ mice (Fig. 3G). As such, absence of XBP1 in
318 CD11c-expressing cells results in decreased CD8$^+$ and CD4$^+$ T cell effector function in
319 melanoma tumors. Analysis of the MC38 model showed that whereas the CD8$^+$ T cell
320 response was not affected, there was a significant reduction in the frequencies of IFN-γ-
321 producing and IFN-γ/ TNF-producing CD4$^+$ T cells (Supp. Fig. 4F-G).
322 Impaired cytokine production is a hallmark of CD8$^+$ T cell exhaustion in cancer (41, 42),
323 a process characterized by a progressive loss of function that culminates with the
324 generation of terminal exhausted TIM-3$^+$CD8$^+$ T cells unable to control tumor growth
325 (42). TIM-3$^+$CD8$^+$ T cells do not proliferate, are unresponsive to anti-PD1 therapy (41, 43)
326 and originate from 'precursor exhausted' CD8$^+$ T cells, a T cell state characterized by the
327 expression of the transcription factor TCF-1 (termed 'TCF1$^+$CD8$^+$ T cells'), which retain
328 proliferative potential and can be reinvigorated through anti-PD1 therapy (41, 43, 44).
329 We determined the presence of intratumoral TCF-1$^+$CD8$^+$ T cells and TIM-3$^+$CD8$^+$ T cells
330 in melanoma tumors from XBP1$^{\Delta DC}$ mice and control animals. Tumors from XBP1$^{\Delta DC}$ mice
331 show decreased infiltration of TCF-1$^+$CD8$^+$ T cells and increased proportions of TIM-
332 3$^+$CD8$^+$ T cells compared to tumors from control animals (Figure 3H-I). Additionally,
333 TIM3$^+$ CD8$^+$ T cells from XBP1^{WT} and XBP1$^{\Delta DC}$ mice display a *bona-fide* terminal exhausted
334 phenotype, with elevated levels of CD39, TOX and granzyme B (Supp. Fig. 4H). These

335 findings are consistent with data depicted in figure 3E-F showing lower frequencies of
336 polyfunctional cytokine-producing $CD8^+$ T cells in tumors from $XBP1^{\Delta DC}$ mice, which is an
337 attribute of precursor exhausted $TCF\text{-}1^+CD8^+$ T cells (41). Altogether, our data shows that
338 XBP1s in the $CD11c^+$ compartment coordinates the balance of $CD8^+$ T cell profiles in
339 melanoma.
340

341 **Tumor cDC1s from $XBP1^{\Delta DC}$ mice display signs of RIDD**

342 Thus far, our data indicate that XBP1s expression in DCs modulates melanoma tumor
343 growth and the balance of effector and exhausted T cell subsets. However, it is unclear if
344 these processes depend on XBP1s-transcriptional activity, as previous work
345 demonstrated that XBP1s deficiency leads to hyperactivation of IRE1 RNase and RIDD in
346 steady state cDC1s (25, 26). Thus, we interrogated if XBP1 deficiency also resulted in
347 increased IRE1 RNase activity in tumor cDC1s (Fig 4A). We measured expression of *Xbp1*
348 spliced/unspliced mRNA in tumor cDC1s from control and $XBP1^{\Delta DC}$ mice. Although
349 $XBP1^{\Delta DC}$ cDC1s are unable to synthesize XBP1s protein, these cells still generate *Xbp1*
350 mRNA bearing the IRE1 cleavage sites, which serves as an assay to monitor IRE1 RNase
351 activity (26). Data in Figure 4B show that tumor cDC1s isolated from $XBP1^{\Delta DC}$ mice
352 express marked levels of *Xbp1s* mRNA compared to control counterparts, which is an
353 indicative sign of IRE1 RNase hyperactivation.
354 To determine RIDD on protein level in tumor DCs, we determined surface expression of
355 the integrin CD11c, a dimeric partner of *Itgb2* (coding the integrin CD18), which is a
356 reported mRNA substrate of IRE1 RNase (26). CD11c surface expression depends on
357 RIDD-mediated degradation of *Itgb2* mRNA and therefore, it can be used as a surrogate
358 marker for RIDD activity. Data in Fig. 4C show that tumor cDC1s from $XBP1^{\Delta DC}$ express
359 lower surface levels of CD11c than control counterparts, confirming RIDD induction on

360 protein level. Similar effect was observed in cDC1 subsets from the TdLN (Fig 4D). These
361 data show that XBP1-deficient cDC1s display signs of RIDD in melanoma tumors.
362 Interestingly, additional APCs such as tumor cDC2s and TAM from XBP1$^{\Delta DC}$ mice showed
363 a modest but noticeable reduction in CD11c expression (Fig. 4C), suggesting that these
364 cells may also induce RIDD upon XBP1 loss, albeit at lower extent than cDC1s.
365
366 **Gene expression profiles of tumor cDC1s deficient for IRE1 RNase and XBP1**
367 Given that XBP1 deficient cDC1s show signs of RIDD at the tumor site, we analyzed the
368 transcriptomic signature downstream of IRE1 RNase in melanoma-infiltrating cDC1s. To
369 identify specific XBP1-dependent and RIDD-dependent targets, we carried out a parallel
370 analysis of the transcriptome of tumor cDC1s deficient for XBP1, or double deficient for
371 the RNase domain of IRE1 and XBP1. To generate double *knock-out* animals for the IRE1
372 RNase and XBP1 in CD11c-expressing cells, we crossed XBP1$^{\Delta DC}$ mice with *Ern1*$^{fl/fl}$ mice,
373 which bear loxP sites flanking exon 20 and 21 of the *Ern1* gene and generates a truncated
374 IRE1 isoform lacking the RNase domain (45) (referred to as "XBP1$^{\Delta DC}$/IRE1^{trunc}DC mice").
375 As such, XBP1$^{\Delta DC}$ mice lack the transcription factor and activate RIDD, whereas double
376 deficient XBP1$^{\Delta DC}$/IRE1^{trunc}DC mice lack both XBP1s and RIDD (Supp. Fig 5A-C). With this
377 strategy, XBP1s target genes are identified as transcripts that are downregulated in tumor
378 cDC1s from both XBP1$^{\Delta DC}$ and XBP1$^{\Delta DC}$/IRE1^{trunc}DC mice. In contrast, RIDD-dependent
379 transcripts are recognized as mRNAs that decrease their expression in XBP1-deficient
380 tumor cDC1s, but which expression is restored in XBP1$^{\Delta DC}$/IRE1^{trunc}DC animals.
381 Tumor cDC1s were isolated by cell sorting from B16 melanoma tumors of control,
382 XBP1$^{\Delta DC}$ or XBP1$^{\Delta DC}$/IRE1^{trunc}DC mice and the transcriptome was analyzed by bulk RNA
383 sequencing (RNA-seq). 51 differentially expressed genes (DEG) were identified among
384 XBP1$^{\Delta DC}$ or XBP1$^{\Delta DC}$/IRE1^{trunc}DC cDC1s (adjusted p-value < 0.05 and |Fold Change| > 1.5)

385 (Fig. 5A). Biological pathway enrichment analysis using Gene Ontology (GO)
386 knowledgebase revealed that a large proportion of DEGs are constituents of the response
387 to misfolded proteins and transport and localization of ER proteins (see Biological
388 Process, Fig. 5B). There was also an overrepresentation of protein disulfide-isomerases
389 (see Molecular Function, Fig. 5B) and on intracellular localization level, most deregulated
390 genes encoded ER proteins (see Cellular Component, Fig. 5B). Next, we analyzed the DEGs
391 per mice line, which clustered these genes into three main groups: (1) genes upregulated
392 in XBP1-deficient and IRE1 RNase/XBP1-deficient tumor cDC1s; (2) genes
393 downregulated in both XBP1-deficient and IRE1 RNase/XBP1-deficient tumor cDC1s
394 (XBP1s targets); and (3) genes downregulated exclusively in XBP1-deficient tumor cDC1s
395 (potential RIDD targets) (Fig. 5A). In group (1), we identified five transcripts including
396 *Hspa5* which encodes BiP, a chaperone induced upon UPR activation (46). This finding
397 indicates that XBP1-deficient and IRE1 RNase/XBP1-double deficient tumor cDC1s show
398 signs of ER stress (Fig. 5A). We also identified *Cox6a2* (subunit of cytochrome C oxidase),
399 which was previously identified as an upregulated gene in XBP1-deficient cDC1s (26).
400 Transcripts in group (2) include protein disulfide isomerases (*Erp44, Txndx11, Txndc5,*
401 *P4hb*) chaperones (*Dnajb9/Hyou1*); glycosylation proteins (*Rpn1, Alg2, Serp1*), proteins
402 involved in transport to the ER (*Sec61a1, Sec61b, Spcs2, Spcs3, Ssr3*) and from the ER to
403 Golgi (*Bet1, Surf4*) (Fig. 5A). Additional canonical XBP1s targets (*Stt3a* and *Edem2)* were
404 identified when the cut off value was set below 1.5-fold (Supp. Fig 6A). Gene Set
405 Enrichment Analysis (GSEA) revealed that the transcriptome of both XBP1$^{\Delta DC}$ and
406 XBP1$^{\Delta DC}$/IRE1^{trunc}DC tumor cDC1s were depleted of targets related to protein
407 glycosylation, ER to Golgi transport, protein localization to the ER and lipid biosynthesis
408 (Fig 5C-D).

409 Finally, group (3) includes the canonical RIDD substrates *Bloc1s1*, *St3gal5* (21), *Itgb2* (26),
410 plus a subset of transcripts with heterogeneous functions (Fig. 5A) that range from lipid
411 synthesis and metabolism members (*St3gal5, Gm2a, Abca2*), Ca^{+2} homeostasis (*Stim2,*
412 *Pkd1*), protein folding (*Qsox1, Mlec*), a steroid binding receptor (*Paqr7*), an amino acid
413 transporter (*Slc1a5*) , a member of the nuclear pore complex (*Nup210*), an E3-ubiquitin
414 ligase (*Rnf130*), signaling receptors in immunity and development (*Fcrla*, *Notch4*,
415 respectively) to *Eif2ak3,* which encodes the UPR transducer PERK. Consistent with the
416 functional heterogeneity of RIDD targets, GSEA did not reveal differences at the level of
417 biological processes between XBP1$^{\Delta DC}$ and XBP1$^{\Delta DC}$/IRE1^{trunc}DC cDC1s (Fig 5C-D). Even
418 though some processes such as antigen processing and presentation and cell-redox
419 homeostasis are downregulated exclusively in tumor cDC1s from XBP1$^{\Delta DC}$ mice (thereby
420 suggesting RIDD dependency), these processes display low enrichment scores. To sum
421 up, these data indicate that tumor cDC1s from XBP1$^{\Delta DC}$ mice display an altered XBP1s
422 transcriptional program related to protein homeostasis and folding, and counter activate
423 RIDD. Using GSEA and reported XBP1s-target and RIDD-target gene datasets (31, 47) we
424 confirmed downregulation of the canonical XBP1s transcription program in both XBP1$^{\Delta DC}$
425 cDC1s and double deficient XBP1$^{\Delta DC}$/IRE1^{trunc}DC cDC1s (Fig 5E-F, Supp. Fig. S6B),
426 whereas RIDD-dependent targets are predominantly downregulated in XBP1$^{\Delta DC}$ cDC1s
427 (Fig 5E-F, Supp Fig. S6B). Finally, our findings reveal that melanoma-infiltrating cDC1s do
428 not show signs of dysfunctional XBP1s activity, as genes related to triglyceride
429 biosynthesis that are associated with diminished DC function in other cancer settings are
430 not downregulated upon XBP1s or IRE1 RNase loss (Supp. Fig. 6C-D) (30). Taken together,
431 these results demonstrate that XBP1 deficiency in tumor cDC1s impairs transcriptomic
432 programs associated with the maintenance of proteostasis and induces RIDD.
433

434 **RIDD activation in DCs accounts for the changes related to tumor growth and**
435 **dysregulated antitumor T cell immunity noticed in XBP1$^{\Delta DC}$ mice**

436 Our observations raise the question as to whether the increased tumor growth and T cell
437 dysregulation noticed in XBP1$^{\Delta DC}$ mice is due to XBP1s- or RIDD-dependent outputs in
438 DCs. To address this issue, we implanted the B78ChOVA cell line in control and
439 XBP1$^{\Delta DC}$/IRE1^{trunc}DC animals (Fig. 6A-B), in which RIDD is abolished (Supp. Fig. 5A-C).
440 Remarkably, in contrast to the observations noticed in XBP1$^{\Delta DC}$ mice (Fig. 2A), the tumor
441 size of animals lacking both XBP1 and IRE1 RNase in DCs was comparable to that
442 observed in control animals (41.78 ± 9.033 vs 53.90 ± 12.36 mm^3, p=0.42, mean ± s.e.m.)
443 (Fig. 6B), indicating that RIDD activation in CD11c-expressing cells accounts for the
444 increased tumor growth. Furthermore, we examined whether the reduced frequencies of
445 cytokine producing CD8$^+$ T cells and the disbalance between TCF-1$^+$/TIM-3$^+$ CD8$^+$ T cells
446 noticed in XBP1$^{\Delta DC}$ mice are also dependent on RIDD. Analysis of tumor-infiltrating CD8$^+$
447 T cells revealed no differences in the frequencies of IFN-γ producing CD8$^+$T cells, TNF
448 producing CD8$^+$T cells, IL-2 producing CD8$^+$T cells, nor in the proportion of double or
449 triple cytokine producers between XBP1$^{\Delta DC}$/IRE1^{trunc}DC mice and control animals (Fig.
450 6C-D). Similar results were observed for IFN-γ producing or double IFN-γ/ TNF-α
451 producing CD4$^+$ T cells (Fig. 6E). In addition, analysis of the composition of precursor-
452 exhausted/terminal exhausted T cells revealed similar infiltration of TCF-1$^+$/TIM-3$^+$ CD8$^+$
453 T cells in melanoma tumors from XBP1$^{\Delta DC}$/IRE1^{trunc}DC mice versus control animals (Fig.
454 6F-G), indicating that IRE1 RNase activity in DCs accounted for the accumulation of
455 dysfunctional CD8$^+$ T cells in melanoma. Altogether, these data indicates that
456 hyperactivation of the RNase domain of IRE1 in DCs fine tunes melanoma tumor growth
457 and antitumor T cell immunity.

458

459 # DISCUSSION

460 The IRE1/XBP1s axis has emerged as a critical regulator of immunity and cancer (27, 48,
461 49). The differential mechanisms by which IRE1 signaling integrates the intensity and
462 duration of ER stress to regulate cell fate is particularly noticed in the immune system,
463 with cells such as cDC1s, B cells, NK cells and eosinophils that opt for an intact
464 IRE1/XBP1s axis to maintain cellular health (25, 31, 50, 51), or cells including TAM/MdCs
465 or intratumoral T cells, which acquire dysfunctional phenotypes upon enforced activation
466 of the UPR sensor (27, 32, 52).

467 Here, we report that loss of XBP1 in CD11c-expressing cells results in increased
468 melanoma tumor growth, decreased frequencies of cytokine-producing T cells and
469 accumulation of terminal exhausted TIM-3^{+}CD8^{+} T cells. Notably, this effect is abrogated
470 in XBP1$^{\Delta DC}$/IRE1^{trunc}DC mice, demonstrating that IRE1 RNase-dependent, XBP1s-
471 independent outputs account for the dysregulated antitumor immunity in melanoma. We
472 also observe a milder phenotype in the MC38 model, suggesting that different tumor
473 models differentially regulate the IRE1/XBP1s axis in DCs.

474 The results presented in this work contrast with previous studies demonstrating that
475 persistent IRE1/XBP1s activation in tumor DCs curtails their antitumor function. In
476 ovarian cancer, the same XBP1$^{\Delta DC}$ mice line show marked inhibition of tumor progression
477 and improved antitumor immunity (30). One possibility accounting for these differences
478 may be related to the different composition of DCs infiltrating these cancer models. In
479 ovarian cancer models, tumor-associated DCs are spontaneously immunosuppressive
480 (53) and in fact, whereas depletion of CD11c^{+} cells delays ovarian cancer progression in
481 later stages (54), the same process curtails CD8^{+} T cell priming in melanoma (55).
482 Furthermore, XBP1 deficiency in ovarian cancer DCs does not lead to RIDD activation
483 (30), which contrasts to the evidence presented in this work. Thus, as result of these

484 combined data, we must consider that the outcome of the IRE1 outputs in tumor DCs may
485 drastically differ depending on the DC subset and the cancer type. In fact, data presented
486 here show that animals lacking both XBP1 and IRE1 RNase in DCs display normal
487 melanoma tumor growth and T cell immunity, indicating that the deletion of an entire
488 branch of the UPR in DCs does not have a predetermined role across different tumor types.
489 These results complement existing literature and may be relevant for building a
490 comprehensive understanding on future manipulation of the IRE1/XBP1s axis in cancer.
491 In addition, even though we use a genetic model of XBP1 deletion to reveal the scope of
492 RIDD in tumor DCs which may not recapitulate physiological responses, our work alludes
493 to cDC1s as regulators of anti-melanoma T cell immunity in XBP1$^{\Delta DC}$ mice. First, cDC1s are
494 the subset with the highest IRE1 RNase activity within melanoma and MC38 tumor niches,
495 and T cell parameters altered by XBP1 loss in CD11c^{+} cells, such as the induction of
496 intratumoral IFN-γ producing CD8^{+} T cells and the maintenance of precursor exhausted
497 TCF1^{+}CD8^{+} T cells are attributed to cDC1 function (8, 11). Furthermore, these processes
498 are also dependent on RIDD activation by DCs, which is more strongly induced in cDC1s
499 from XBP1$^{\Delta DC}$ mice (25, 26). Nevertheless, as we also observe reduced frequencies of
500 tumor infiltrating CD4^{+} IFNγ^{+} T cells in XBP1$^{\Delta DC}$ mice in melanoma and MC38 models, a
501 contribution of IRE1 RNase in CD4^{+} T cell priming by tumor cDC1s (56) or also by cDC2s
502 (17) cannot be excluded.
503 On a mechanistic level, we do not find a role for IRE1 RNase in cross-presentation of tumor
504 antigens, contrasting with previous findings in steady state cDC1s (26). These data
505 suggest that tumors may shape the spectra of XBP1s/RIDD targets in infiltrating cDC1s or
506 that additional mechanisms (or DC subtypes) may compensate for the process. In fact,
507 *tapbp* mRNA, a previously identified RIDD target in XBP1-deficient splenic DCs
508 contributing to antigen cross-presentation is not found as DEG in the transcriptomic

509 analysis of this study. In addition, growing evidence demonstrating the capacity of tumor
510 DCs to carry out cross-dressing of MHC-I/peptide complexes from tumor cells adds a new
511 layer of complexity that remains to be addressed (57, 58). However, one novel candidate
512 identified in this analysis as a potential RIDD substrate, the ER-resident FC receptor Like
513 A (*Fcrla)* (Fig. 5A), has been previously identified as part of a BATF3/IRF8 transcriptional
514 program that confers tumor immunogenicity in cDC1s independently of cross-
515 presentation (59). As such, data presented here delineates for first time the XBP1s-
516 dependent and RIDD-dependent targets in tumor cDC1s, which may serve as basis for
517 future studies focused on addressing the role of selective IRE1 RNase targets involved in
518 the regulation of antitumor immunity.
519 Multiple efforts are currently focused on the development of pharmacological compounds
520 targeting the IRE1 RNase active site and XBP1s *in vivo*, many of which have shown
521 translational potential in cancer (60). A recent study revealed that RIDD regulates
522 expression of the MHC-I heavy chain mRNAs in DCs and that inhibition of IRE1 RNase
523 through systemic administration of small molecules greatly attenuates tumor growth in
524 4T1 and CT26 models, by a mechanism proposed to be dependent on DC cross-
525 presentation (61). Even though we do not find MHC-I heavy chain mRNAs as DEGs in the
526 transcriptomic analysis of tumor cDC1s from XBP1$^{\Delta DC}$/IRE1^{trunc}DC mice, and we do not
527 find an improved melanoma tumor response in XBP1$^{\Delta DC}$/IRE1^{trunc}DC animals, future
528 studies are required to integrate these findings through experiments that include kinetics
529 of comparable tumor models. Finally, the work presented here serves as a proof-of-
530 concept study demonstrating that IRE1 RNase dependent, XBP1s-independent outputs in
531 DCs may also contribute to fine-tuning antitumor immunity.
532
533

534 # MATERIAL AND METHODS

535 **RESOURCE AVAILABILITY**

536 Further information and requests for resources and reagents should be directed to
537 Fabiola Osorio (fabiolaosorio@med.uchile.cl).

538

539 ***Materials availability***

540 This study did not generate new unique reagents.

541

542 ***Data and code availability***

543 RNA-seq data have been deposited at GEO and are publicly available as of the date of
544 publication. Accession numbers are listed in supplementary resources table. This paper
545 does not report original code. Any additional information required to reanalyze the data
546 reported in this paper is available upon request.

547

548 **EXPERIMENTAL MODEL AND SUBJECT DETAILS**

549 ***Mice***

550 ERAI (33), XBP1^{WT}(XBP1fl/fl (36)), XBP1$^{\Delta DC}$ (XBP1fl/fl x CD11c-Cre (37)),
551 XBP1^{WT}/IRE1^{WT} (XBP1fl/fl x IRE1fl/fl (45)), XBP1$^{\Delta DC}$ IRE1^{trunc}DC (XBP1fl/fl x IRE1fl/fl x
552 CD11c-Cre) mice were bred at Universidad de Chile and Fundación Ciencia y Vida in
553 specific pathogen-free conditions. Also, for RNA seq studies XBP1^{WT}, XBP1$^{\Delta DC}$,
554 XBP1^{WT}/IRE1^{WT} and XBP1$^{\Delta DC}$ IRE1^{trunc}DC mice were bred at the animal facility at VIB
555 institute. pmel-1 mice (40) were kindly donated by Dr F. Salazar-Onfray. All mice were
556 kept on a C57BL/6 background. Litters with mice of both sexes at 6–14 weeks of age were
557 used for experiments.

558

559 ***Cell Lines***

560 B78-ChOVA cells were kindly provided by Dr. Matthew Krummel (UCSF) (2). B16-F10
561 cells were obtained from ATCG (#CRL-6475). B16-FLT3L cell line (62) was provided by
562 Dr. Maria Rosa Bono (University of Chile). MC-38 cell line was provided by Dr. Álvaro
563 Lladser (Universidad San Sebastian). Cells were cultured under standard conditions prior
564 to injection into mice. Briefly, cells were cultured in DMEM (B78-ChOVA) or RPMI-1640
565 (B16-F10/B16-FLT3L/MC-38) supplemented with 10% v/v inactivated fetal bovine
566 serum (FBS, Gibco), 100 U/mL penicillin (Corning), 100 µg/mL streptomycin (Corning)
567 and 0.55 mM 2-Mercaptoethanol (Gibco). For MC-38 culture, media was supplemented
568 additionally with non-essential amino acids (ThermoFisher Scientific) and 1 mM sodium
569 pyruvate (ThermoFisher Scientific). Cells were cultured on T75 tissue-culture treated
570 plastic flasks at 37°C, 5% CO_2. Cells were split every other day.

571

572 **METHOD DETAILS**

573 ***Tumor Model***

574 Tumor cell lines were harvested, washed with PBS, and resuspended in a final injection
575 volume of 50 µl PBS. $5x10^5$ (B16/B78-ChOVA) or $1x10^6$ (MC-38) tumor cells were injected
576 in the right flank of shaved mice intradermally and allowed to grow for 10-15 days. For
577 tumor growth curves, tumor size was determined by two orthogonal measurements with
578 a caliper and the volume was estimated as (width^2 x length)/2.

579

580 ***Preparation of Cell Suspensions***

581 Tumors were minced and digested with Collagenase D (1 mg/mL, Roche) and DNAse I (50
582 µg/mL, Roche) for 30 minutes at 37°C in a water bath. Digested tissue was then passed
583 through a 70 µm cell strainer, followed by red blood cell lysis with RBC lysis buffer
584 (Biolegend). Single cells were kept on ice.
585 For whole intratumoral immune cell profiling and DC stainings, CD45-biotin magnetic
586 positive selection (MACS, Miltenyi) was performed to enrich for total tumor immune
587 infiltrate.
588 For intratumoral T cell stainings, hematopoietic cells were enriched by density gradient
589 centrifugation with 40/70 Percoll (GE Healthcare) for 20 min at 700xg.
590 Tumor draining lymph nodes (tdLNs) were minced and digested with Collagenase D (1
591 mg/mL, Roche) and DNAse I (50 µg/mL, Roche) for 45 minutes at 37°C in a water bath.
592 Digested tissue was then passed through a 70 µm cell strainer and single cells were kept
593 on ice.
594
595 ***Bone marrow derived DCs generation***
596 Bone marrow cells from femurs and tibias were cultured in presence of 20 ng/ml mouse
597 recombinant GM-CSF (Biolegend) for 8 days. Fresh culture medium with cytokine was
598 added on day 3, and on day 6. After harvesting and when indicated, cells were stimulated
599 with 1 ug/mL Tunicamycin (Sigma) for 8h followed by total RNA extraction with Trizol
600 (Invitrogen).
601
602 ***Bone marrow derived cDC1s generation and tumor lysate stimulation***
603 Bone marrow cells from femurs and tibias were cultured in presence of 100 ng/ml
604 recombinant human FLT3-L (Peprotech). After three days of differentiation, cells were

605 plated onto a monolayer of OP9-DL1 stromal cells and co-cultured for additional 6 days
606 as reported (38, 39).
607
608 For tumor lysate preparation B78-ChOVA cells were washed twice with PBS, resuspended
609 at $8x10^6$ cells/mL in RPMI supplemented with 10% FBS and aliquoted in cryotubes. Cell
610 suspensions were subjected to heat-shock (42°C for 60 min) followed by three cycles of
611 freeze/thaw (liquid nitrogen/waterbath at 37°C). Tumor lysates were stored at -80°C
612 until use.
613 BM-derived cDC1s were harvested and plated with B78-ChOVA lysates (50 uL/mL) in
614 round-bottom p96 plates. After 14h, Brefeldin A (GolgiPlug, BD) was added and four
615 hours later, cells were harvested and stained for intracellular IL-12p40 expression by
616 flow cytometry.
617
618 ***Xbp1s splicing assay***
619 Total RNA was isolated either by Trizol (Invitrogen) or RNAeasy plus Micro Kit (Qiagen).
620 cDNA was prepared using M-MLV reverse transcriptase (Invitrogen). The following
621 primers were used for conventional PCR amplification of total Xbp1: Fwd: 5'-
622 ACACGCTTGGGAATGGACAC-3' and Rev: 5'-CCATGGGAAGATGTTCTGGG-3' (26); and for
623 beta actin (*Actb*): Fwd: 5'-CTAAGGCCAACCGTGAAAAG-3' and Rev: 5'-
624 TTGCTGATCCACATCTGCTG-3' or alternatively for beta actin (*Actb*): Fwd 5'-
625 GTGACGTTGACATCCGTAAAGA-3' and Rev: 5'-GCCGGACTCATCGTACTCC-3'. PCR
626 products were analyzed on agarose gels.
627
628 ***Flow Cytometry and Cell Sorting***

629 For surface staining, cells were incubated with anti-Fc receptor antibody (anti-CD16/32,
630 Biolegend) and then stained with fluorochrome-conjugated antibodies in FACS buffer
631 (PBS + 1% FBS + 2mM EDTA) for 30 min at 4°C. Viability was assessed by staining with
632 fixable viability Zombie (BioLegend) or LIVE/DEAD fixable (Invitrogen). A biotinylated
633 antibody was used for F4/80 staining, followed by a second staining step with
634 Streptoavidin-APC (Biolegend) for 30 min at 4°C. Flow cytometry was performed on BD
635 Fortessa LSR instrument. Analysis of flow cytometry data was done using FlowJo
636 software. Cell sorting was performed using a BD FACS Aria III.
637
638 ***Transcription Factors and Granzyme B intracellular staining***
639 After surface staining, cells were fixed and permeabilized using Foxp3 transcription factor
640 staining set (eBioscience) followed by intracellular staining of transcription factors
641 (Foxp3, Tcf1, Tox) and/or granzyme B as indicated by the manufacturer protocol.
642
643 ***T cell stimulation and intracellular cytokine staining***
644 Tumor and TdLN cell suspensions were stimulated *ex-vivo* prior to staining with 0.25 μM
645 phorbol 12- myristate 13-acetate (PMA; Sigma) and 1 μg/mL Ionomycin (Sigma) at 37°C
646 and 5% CO_2 for 3.5 hr in the presence of Brefeldin A (BD GolgiPlug). After stimulation,
647 cells were surface stained as mentioned above. Then, cells were fixed and permeabilized
648 using BD Cytofix/Cytoperm fixation/permeabilization kit (BD) followed by intracellular
649 staining of cytokines (IFN-γ, IL-2 and TNF-α) as indicated by the manufacturer protocol.
650
651 ***Tetramer staining***

652 For OVA-specific CD8+ T cell quantification cells were incubated with PE H2-K^b-OVA
653 (SIINFEKL) tetramers (MBL) at room temperature for 30 min protected from light,
654 followed by surface staining and FACS analysis.
655
656 ***t-SNE and clustering***
657 For tSNE visualization of tumor immune infiltrate a multicolor flow cytometry panel was
658 used including 19 parameters (FSC, SSC, Viability, CD45, VenusFP, XCR1, CD4, NK1.1,
659 CD26, F4/80, Ly6G, MHCII, CD24, CD3e, Ly6C, CD8a, CD11c, CD11b, CD19). Cells were
660 compensated for spillover between channels and pre-gated on CD45+ Live singlets using
661 FlowJo. Flowjo workspace was imported into the R environment using CytoML v2.4.0 ,
662 FlowWokspace v4.4.0 and FlowCore v2.4.0 packages (63–65). The intensity values of
663 marker expression were then biexp-transformed via the flowjo_biexp_trans function of
664 FlowWorkspace using parameters ChannelRange=4096, maxValue=262144, pos=4.5,
665 neg=0 and widthBasis=-10. Subsequently 5.000 cell events from each mouse (4 WT and 4
666 ERAI) were randomly sampled and combined for a total of 40.000 single cells. Sampled
667 data was min-max normalized, and subjected to dimensionality reduction by Barnes-
668 Hutts implementation of t-Distributed Stochastic Neighbor Embedding (tSNE) using
669 RtSNE v0.15 package (66). Thirteen parameters were used for tSNE construction (XCR1,
670 CD4, NK1.1, CD26, F4/80, Ly6G, MHCII, CD24, CD3e, Ly6C, CD8a, CD11c, CD11b and CD19)
671 and the parameters were set to iterations=1000 and perplexity =30. After dimensionality
672 reduction, automatic clustering was performed using density based spatial clustering
673 (DBSCAN) using DBSCAN v1.1.8 package (67). Dotplot for marker expression among
674 clusters and Violin plots for VenusFP were then generated using ggplot2 v3.3.5 package
675 (68).
676

677 ***In vivo T cell proliferation assay***

678 LN cells from pmel-1 TCR transgenic mice were isolated and enriched for CD8+ T cells by
679 magnetic negative selection using CD8+ T cell isolation kit (MACS, Miltenyi). Enriched
680 CD8+ T cells were surface stained and naïve CD8+ T cells were purified by cell sorting
681 (CD8a+, CD62L high, CD44low, CD25 neg). After sorting, naïve CD8+ T cells were labeled
682 with Cell Trace Violet (CTV, Invitrogen). $1x10^6$ naïve CD8+ T cells were adoptively
683 transferred into B16-F10 tumor-bearing mice at day 7 after tumor challenge. *In vivo*
684 proliferation and CD44/CD25 expression of transferred T cells was analyzed by FACS in
685 tumor draining lymph nodes 4 days after adoptive transfer.

686

687 ***RNA-seq***

688 Cell suspensions from tumor tissue pooled from 2-4 B16 bearing mice were enriched in
689 immune cells by positive selection with CD45+ biotin magnetic beads (MACS, Miltenyi).
690 Enriched cells were surface stained and 5-20 $x10^3$ intratumoral cDC1s were sorted
691 directly in RLT lysis buffer (Qiagen) containing 2-mercaptoethanol. Immediately after
692 sorting, collected cells were homogenized through vortex and frozen on dry ice before
693 storage at -80°C. Total RNA was extracted with RNAeasy Plus Micro kit (Qiagen). RNA
694 sequencing was performed at VIB Nucleomics Core using SMART-seq v4 pre-
695 amplification followed by single-end sequencing on Illumina NextSeq500. Preprocessing
696 of the RNA-seq data was performed by Trimmomatic v0.39 and quality control by FastQC
697 v0.11.8. Mapping to the reference mouse genome was performed by STAR v2.7.3a and
698 HTSeqCount v0.11.2 was used for counting. Limma v3.42.2 (69) was used to normalize
699 the data. Genes which did not meet the requirement of a count per million (cpm) value
700 larger than 1 in at least 4 samples were filtered. This resulted in an expression table
701 containing 11066 genes. EdgeR v3.28.0 (70) was utilized to perform differential

702 expression analysis. Benjamini-Hochberg correction was used to adjust the p-values for
703 multiple testing. Differentially expressed genes were filtered as genes with a |FC| > 1.5
704 and adjusted p-value < 0.05. Heatmaps were created using pheatmap v1.0.12 package
705 (71) on log2 normalized and mean centered gene expression data.
706
707 ***Gene Set Enrichment Analysis***
708 Over-Representation Analysis (ORA) and Gene Set Enrichment Analysis (GSEA) were
709 performed using *ClusterProfiler* v4.0.5 package (72) in R and Gene Ontology (GO)
710 knowledgebase gene sets. ORA results were considered significant when the q-value was
711 below 0.01. GSEA was performed on pre-ranked mode using as rank metric the signed
712 log10 transformed p-values derived from the differential expression analysis. GSEA was
713 run using the GO:BP database or literature lists of Xbp1-targets and RIDD-targets (47).
714 Results were considered significant when the adjusted p-value was below 0.05.
715
716 **QUANTIFICATION AND STATISTICAL ANALYSIS**
717 No statistical methods were used to predetermine sample size. The experiments were
718 not randomized, and the investigators were not blinded to allocation during
719 experiments and outcome assessment. Statistical analysis was conducted using
720 GraphPad Prism software (v9.1.2). Results are presented as mean ± SEM. Two groups
721 were compared using two tailed t-test for normal distributed data (Shapiro-Wilk test) or
722 using a non-parametric two-tailed Mann-Whitney test as indicated in figure legends.
723 Multiple groups were compared using one-way ANOVA with Tukey post-test. A p-value
724 < 0.05 was considered statistically significant.
725
726 **STUDY APPROVAL**

727 All animal procedures were performed in accordance with institutional guidelines for
728 animal care of the Fundación Ciencia y Vida, the Faculty of Medicine, University of Chile
729 and the VIB, Belgium, and were approved by the local ethics committee.
730
731
732
733
734
735
736
737
738
739
740
741
742
743
744
745

746 ## Author contributions

747 F.F, MR.B, S.J and F.O designed the research; F.F, S.R, S.G, C.F, D.F did the experiments. F.F,
748 S.R, S.J and F.O analyzed the results; C.DN and C.M helped with RNA-seq data analysis;
749 D.Fe provided technical assistance and experimental expertise, T.I and A.L provided
750 critical reagents. F.F. and F.O wrote the manuscript

751

752 ## Acknowledgements

753 We thank Dr Laurie H. Glimcher (Dana-Farber Cancer Institute) for *Xbp1*$^{fl/fl}$ mice; Dr
754 Matthew Krummel (UCSF) for the B78ChOVA cell line; the VIB nucleomics facility for
755 doing the RNA seq experiments and facilities at Universidad de Chile and Fundación
756 Ciencia & Vida. We thank members of the immunology and immunology and cellular
757 stress laboratories for critical support.
758 This work was funded by an International Research Scholar grant from HHMI
759 (HHMI#55008744, FO); FONDECYT grant No 1200793 (FO); FONDECYT grant No
760 1191438 (MR.B); CONICYT/FONDEQUIP/EQM140016; FONDECYT grant No 1212070
761 (AL); ANID grant FB210008 (MR.B and AL); CONICYT-PFCHA/DoctoradoNacional/2017-
762 21170366 (F.F). The work in Belgium was funded by Stichting tegen Kanker (2014/283),
763 FWO-EOS (ID 30837538) and ERC-CoG (ID 819314) (S.J.).

764

765 ## Declaration of interest

766 The authors declare no competing interests.

767

768

769

770 # FIGURE LEGENDS

771 **Figure 1. cDC1s are predominant cellular targets of IRE1 activation in melanoma**
772 **tumors**.

773 **(A-F)** B16-F10 melanoma cells were implanted intradermally on ERAI or control mice
774 and 11 days after implantation, tumor tissue was analyzed by multicolor flow cytometry.
775 n=4 mice per group, representative of two independent experiments. **(A)** t-SNE of
776 40.000 immune (CD45+) infiltrating cells from melanoma of ERAI or control mice.
777 Colors indicate unsupervised clustering by DBSCAN. **(B)** Marker expression across the
778 different cell clusters identified in (A). See also Supp. Fig 1A. **(C)** t-SNE map colored by
779 VenusFP signal intensity from control or ERAI mice. cDC1 cluster is highlighted in a red
780 circle. **(D)** VenusFP signal quantification across the different cell clusters identified in
781 (A). Median fluorescence intensity for VenusFP is depicted with a "+" inside each violin
782 plot. **(E-F)** Histograms (E) and quantification (F) of VenusFP signal from manually gated
783 immune populations from B16-F10-bearing WT and ERAI mice (see gating strategy in
784 Supp. Fig.2A). Statistical significance is depicted as compact letter display, ANOVA and
785 Tukey post-test between ERAI mice. **(G-H)** Xbp1 splicing assay (G) of tumor cDC1s
786 isolated by cell sorting from B16-FLT3L-bearing WT mice compared to BMDCs treated
787 with 1 μg/mL of the ER-stressor Tunicamycin (Tun) or medium for 8h. (H) Bars show
788 the image quantification of the ratio between Xbp1 spliced (Xbp1s) and total Xbp1
789 (Xbp1s + Xbp1u). n= 3 samples per group (representative of three independent
790 experiments), mean ± s.e.m, ANOVA and Tukey post-test, ** $p<0.01$, *** $p<0.001$. **(I)**
791 Quantification of VenusFP signal from tumor and tumor draining lymph node migratory
792 (mig) and resident (res) cDCs (see gating strategy in Supp. Fig.2B). ** $p<0.01$, ANOVA
793 and Tukey post-test between ERAI mice. n=4 mice per group, representative of two
794 independent experiments, mean ± s.e.m. **(J)** Quantification of VenusFP signal from

795 intratumoral and spleen monocytes (CD11b^{hi} Ly6C^{hi} cells). *** p<0.001, t-test between
796 ERAI mice. n= 3 mice (ERAI) or 1 mouse (WT), representative of two independent
797 experiments, mean ± s.e.m.
798
799 **Figure 2. XBP1 deletion in CD11c-expressing cells results in increased melanoma**
800 **tumor growth**
801 XBP1^{WT} and XBP1$^{\Delta DC}$ mice were implanted with B78ChOVA tumors. **(A)** Tumor growth
802 curves monitored over a period of 12 days. n=19 mice per group. Pooled data from 4
803 independent experiments. **(B)** Tumor size at day 12 post implantation. * p<0.05, two-
804 tailed t-test. n= 51 mice (XBP1^{WT}) or 53 mice (XBP1$^{\Delta DC}$) from animals used throughout
805 this study (pooled data from 12 independent experiments), boxplot. **(C)** Cell counts for
806 tumor immune infiltrate (CD45+). n=31 mice (XBP1^{WT}) or 29 mice (XBP1$^{\Delta DC}$), pooled
807 data from 8 independent experiments, mean ± s.e.m. **(D)** Frequencies of intratumoral
808 cDC subsets. n=5-10, pooled data from two (cDC2) or three (cDC1) independent
809 experiments, mean ± s.e.m. (E) Frequencies of cDC subsets in TdLN. n=4 mice per group,
810 representative of two independent experiments, mean ± s.e.m. **(F-G)** Frequencies of
811 tumor lymphoid and myeloid populations. n=3-12 mice per group, pooled data from two
812 (neutrophils, TAMs, NK) or three (MdCs, T) independent experiments, mean ± s.e.m. **(H)**
813 Tumor Treg (CD3$^+$CD4$^+$Foxp3$^+$), Tconv (CD3$^+$CD4$^+$Foxp3$^-$) and CD8$^+$ T cells (CD3$^+$CD8$^+$)
814 frequencies. n=8 mice per group, pooled data from two independent experiments, mean
815 ± s.e.m.
816
817 **Figure 3. XBP1 deletion in CD11c-expressing cells results in impaired antitumor T**
818 **cell responses and dysbalanced precursor/terminal exhausted T cell ratio.**

819 **(A)** CD40 and PD-L1 expression by tumor cDCs from B78-ChOVA bearing $XBP1^{WT}$ or
820 $XBP1^{\Delta DC}$ mice. n=7 mice per group, pooled data from two independent experiments,
821 mean ± s.e.m. See also TdLN data in Supp. Fig 4A. **(B)** Intracellular IL-12 expression of *in*
822 *vitro* generated cDC1s (FLT3-L/OP9-DL1) upon stimulation with B78-ChOVA lysates.
823 Gated on cDC1s (MHC-II^+ $CD11c^+$ $CD8^+$ $CD11b^-$). *$p < 0.05$, two-tailed Mann-Whitney test.
824 Each dot represents a biological replicate, n=5, data pooled from three independent
825 experiments, mean ± s.e.m. **(C-D)** $Tetramer^+$ CD8+ T cell frequencies in tumor and TdLN
826 from B78-ChOVA bearing $XBP1^{WT}$ or $XBP1^{\Delta DC}$ mice. Gated on $CD3^+CD8^+$ T cells. n=8 mice
827 per group, pooled data from two independent experiments, mean ± s.e.m. **(E-G)**
828 Cytokines expression by tumor $CD8^+$ T cells (E-F) or $CD4^+$ T cells (G) from B78-ChOVA
829 bearing $XBP1^{WT}$ or $XBP1^{\Delta DC}$ mice after ex vivo stimulation with PMA/ION in the
830 presence of BFA. *$p < 0.05$, two-tailed Mann-Whitney test. n=18 mice ($XBP1^{WT}$) or 17
831 mice ($XBP1^{\Delta DC}$), pooled data from 4 independent experiments, mean ± s.e.m. **(H-I)**
832 Precursor exhausted ($PD1^+TCF1^+$ $TIM3^{neg}$) and terminal exhausted ($PD1^+TCF1^{neg}$ $TIM3^+$)
833 $CD8^+$ T cell tumor frequencies from B78-ChOVA bearing $XBP1^{WT}$ or $XBP1^{\Delta DC}$ mice. Gated
834 on $CD3^+CD8^+$ T cells. * $p<0.05$, **$p<0.01$, two-tailed t-test. N=8 mice per group, pooled
835 data from two independent experiments, mean ± s.e.m.
836
837 **Figure 4. Tumor cDC1s from XBP1ΔDC mice display signs of RIDD.**
838 (A) Upon Cre mediated recombination in $XBP1^{fl/fl}$ mice, a premature stop codon is
839 introduced in the *Xbp1* mRNA sequence, preventing the translation of a functional XBP1s
840 protein. XBP1s absence is reported to trigger IRE1 RNase hyperactivation and induce
841 RIDD in certain cell types (26, 36). However, IRE1 RNase activity can still be monitored
842 by determining Xbp1 mRNA splicing ratio. (B) Scheme depicting LoxP sites and IRE1
843 splicing sites at *Xbp1* locus (top) and PCR analysis of Xbp1 splicing in intratumoral

844 cDC1s isolated from B16-bearing XBP1^{WT} and XBP1$^{\Delta DC}$ mice (bottom). Each lane
845 represents different mice. Xbp1u: Xbp1 unspliced; Xbp1s: Xbp1 spliced; Actb: beta actin.
846 (C) CD11c expression by intratumoral cDC1, cDC2 and TAMs from B16-bearing XBP1^{WT}
847 and XBP1$^{\Delta DC}$ mice. Gray histogram depicts unstained control. * $p<0.05$, ** $p<0.01$, ****
848 $p<0.0001$, two-tailed t-test. n=4 mice per group, representative of two independent
849 experiments, mean ± s.e.m. (D) CD11c expression by cDC subsets in the TdLN from B16-
850 bearing XBP1^{WT} and XBP1$^{\Delta DC}$ mice. Gray histogram depicts unstained control. *$p<0.05$,
851 two-tailed Mann-Whitney test. n=4 mice per group, representative of two independent
852 experiments, mean ± s.e.m.
853
854 **Figure 5. Gene expression profiles of tumor cDC1s deficient for IRE1 RNase and**
855 **XBP1.**
856 WT, XBP1$^{\Delta DC}$ and XBP1$^{\Delta DC}$/IRE1^{trunc}DC mice were implanted with B16 tumors. After 12
857 days, tumor cDC1s were isolated by cell sorting and total RNA was sequenced by RNA-
858 seq. **(A)** Heatmap of differentially expressed genes (DEGs). Three groups of genes were
859 identified by the pattern of expression among the three genotypes. **(B)** Over
860 representation analysis of DEGs over the Gene Ontology (GO) database. **(C)** Gene Set
861 Enrichment Analysis (GSEA) of WT vs XBP1$^{\Delta DC}$ cDC1s using GO:Biological Process
862 database. **(D)** GSEA of WT vs XBP1$^{\Delta DC}$/IRE1^{trunc}DC cDC1s using GO:Biological Process
863 database. **(E-F)** GSEA using XBP1s- and RIDD-target gene sets from literature (So et al,
864 2012, Cell Metabolism).
865
866 **Figure 6. RIDD activation in DCs accounts for the changes related to tumor growth**
867 **and dysregulated antitumor T cell immunity noticed in XBP1ΔDC mice.**

868 XBP1^{WT}/IRE1^{WT} and XBP1$^{\Delta DC}$/IRE1^{trunc}DC mice were implanted with B78ChOVA cells.
869 **(A)** Tumor growth curves monitored over a period of 12 days. n=20 mice
870 (XBP1^{WT}/IRE1^{WT}) or 24 mice (XBP1$^{\Delta DC}$/IRE1^{trunc}DC), data pooled from 4 independent
871 experiments. **(B)** Tumor size at day 12 post implantation. n=24 mice (XBP1^{WT}/IRE1^{WT})
872 or 28 mice (XBP1$^{\Delta DC}$/IRE1^{trunc}DC), data pooled from 5 independent experiments, mean ±
873 s.e.m. **(C-D)** Cytokines expression by tumor CD8^{+} T cells after ex vivo stimulation with
874 PMA/Ionomycin in the presence of BFA. Gated on CD3^{+}CD8^{+} T cells. N=9 mice
875 (XBP1^{WT}/IRE1^{WT}) or 11 mice (XBP1$^{\Delta DC}$/IRE1^{trunc}DC), data pooled from three
876 independent experiments, mean ± s.e.m. **(E-F)** Precursor exhausted (PD1^{+}TCF1^{+}
877 TIM3^{neg}) and terminal exhausted (PD1^{+}TCF1^{neg} TIM3^{+}) CD8^{+} T cell tumor frequencies.
878 Gated on CD3^{+}CD8^{+} T cells. n=9 mice (XBP1^{WT}/IRE1^{WT}) or 11 mice
879 (XBP1$^{\Delta DC}$/IRE1^{trunc}DC), data pooled from three independent experiments, mean ± s.e.m.
880

881 # SUPPLEMENTARY FIGURE LEGENDS

882 **Supplementary Figure 1. Immune analysis of melanoma tumors derived from**
883 **ERAI mice.**
884 **(A)** t-SNE map as in figure 1a. Color gradient shows the expression of the indicated
885 marker**. (B)** Quantification of VenusFP signal from manually gated immune populations
886 from MC-38 bearing WT and ERAI mice. **** $p < 0.0001$, ANOVA and Tukey post-test
887 between ERAI mice. n=3 (WT) or 5 (ERAI) mice per group, representative of two
888 independent experiments.(C) Quantification of VenusFP signal of tumor- and spleen-
889 cDC1s from MC-38 bearing WT and ERAI mice. **** $p<0.0001$, t-test between ERAI mice.
890 n=3 (WT) or 5 (ERAI), representative of two independent experiments.
891

892 **Supplementary Figure 2. Gating strategy for tumor associated cDCs.**

893 **(A)** Gating strategy for identification of immune infiltrated populations in tumors.
894 Representative plots from B16 melanoma tumor. **(B)** Gating strategy for identification of
895 migratory (mig) and resident (res) cDC1s and cDC2s in tumor draining lymph node.
896 Representative plots from B16 melanoma TdLN.

897

898 **Supplementary Figure 3. Tumor growth and T cell infiltration in MC-38 bearing**
899 **XBP1$^{\Delta DC}$ mice.**

900 XBP1^{WT} and XBP1$^{\Delta DC}$ mice were implanted with MC-38 tumors. **(A-C)** Tumor volume
901 curves (A), tumor volumes (B) at end point and tumor weight (C) at end point. n=12-13
902 mice per group. Pooled data from two independent experiments.

903

904 **Supplementary Figure 4. Tumor immune cell analysis of XBP1$^{\Delta DC}$ mice.**

905 **(A)** Related to figure 3A. CD40 and PD-L1 expression by TdLN cDCs**.** n=7 mice per group,
906 pooled data from two independent experiments, mean ± s.e.m. **(B)** Related to figure 3B.
907 Dot plots of IL-12 intracellular expression by *in vitro* generated cDC1s stimulated with
908 B78-ChOVA lysates**. (C)** Related to figure 3C-D. Fluorescence minus one (FMO) and
909 tumor-free WT mouse as negative controls for tetramer staining. **(D-E)** XBP1^{WT} and
910 XBP1$^{\Delta DC}$ mice were implanted with B16-F10 tumors. Seven days after implantation,
911 CD8^{+} naïve T cells isolated from pmel1 transgenic mice were labeled with Cell Trace
912 Violet and were adoptively transferred into tumor-bearing mice. Four days later,
913 transferred cell proliferation and CD44/CD25 expression was quantified by FACS. n=8
914 mice (XBP1^{WT}) or 15 mice (XBP1$^{\Delta DC}$), data pooled from two independent experiments,
915 mean ± s.e.m. **(F-G)** CD8+ T cell (F) and CD4+ T cell (G) frequencies and profiles in MC-
916 38 bearing XBP1^{WT} and XBP1$^{\Delta DC}$ mice. n=11-13, pooled data from two independent

917 experiments, mean ± s.e.m. **(H)** Related to figure 3H-I. Representative histograms of
918 different markers associated with terminal exhausted $CD8^+$ T cells. Gated on
919 $CD3^+CD8^+PD1^+TCF1^+$ or $CD3^+CD8^+PD1^+TIM3^+$ as shown in figure 3H.
920

921 **Supplementary Figure 5. IRE1/XBP1s double deficient cDC1s are unable to**
922 **activate RIDD.**

923 **(A)** PCR analysis of Xbp1 splicing in intratumoral cDC1s isolated from B16-bearing
924 $XBP1^{WT}/IRE1^{WT}$ vs $XBP1^{\Delta DC}/IRE1^{trunc}DC$ mice. Each lane represents different mice.
925 Xbp1u: Xbp1 unspliced; Xbp1s: Xbp1 spliced; Actb: beta actin. **(B)** CD11c expression by
926 intratumoral cDC1, cDC2 and TAMs from B16-bearing $XBP1^{WT}/IRE1^{WT}$ vs
927 $XBP1^{\Delta DC}/IRE1^{trunc}DC$ mice. n=4 mice per group, mean ± s.e.m. **(C)** CD11c expression by
928 cDC subsets in the TdLN from B16-bearing $XBP1^{WT}/IRE1^{WT}$ vs $XBP1^{\Delta DC}/IRE1^{trunc}DC$ mice.
929 *$p<0.05$, two-tailed Mann-Whitney test. n=4 mice per group, mean ± s.e.m.
930

931 **Supplementary Figure 6. RNAseq analysis of WT, XBP1 deficient WT vs IRE1/XBP1**
932 **double deficient cDC1s.**

933 **(A)** Heatmap of genes with an adjusted p-value < 0.05 but with a fold change (FC) below
934 the 1.5 threshold. Table summarize log2FC and adj p-values for WT vs XBP1 and WT vs
935 IRE1/XBP1 deficient cDC1s. **(B)** Related to figure 5F-G. GSEA using XBP1s- and RIDD-
936 target gene sets from literature (So et al, 2012, Cell Metabolism). **(C)** GSEA of the
937 "triglyceride biosynthetic process" gene set (GO: 0019432) in WT vs $XBP1^{\Delta DC}$ cDC1s
938 (left) or WT vs $XBP1^{\Delta DC}/IRE1^{trunc}DC$ cDC1s (right) showing not statistically significant
939 enrichment (q-value > 0.05). **(D)** Normalized expression (z-scores) for genes of the
940 "triglyceride biosynthetic process" gene set (GO: 0019432) in WT, $XBP1^{\Delta DC}$, or
941 $XBP1^{\Delta DC}/IRE1^{trunc}DC$ cDC1s.

942 # REFERENCES

943 1. Hildner K et al. Batf3 Deficiency Reveals a Critical Role for CD8 + Dendritic Cells in
944 Cytotoxic T Cell Immunity. *Science* 2008;322(5904):1097–1100.

945 2. Broz ML et al. Dissecting the Tumor Myeloid Compartment Reveals Rare Activating
946 Antigen-Presenting Cells Critical for T Cell Immunity. *Cancer Cell* 2014;26(5):638–652.

947 3. Roberts EW et al. Critical Role for CD103+/CD141+ Dendritic Cells Bearing CCR7 for
948 Tumor Antigen Trafficking and Priming of T Cell Immunity in Melanoma. *Cancer Cell*
949 2016;30(2):324–336.

950 4. Spranger S, Dai D, Horton B, Gajewski TF. Tumor-Residing Batf3 Dendritic Cells Are
951 Required for Effector T Cell Trafficking and Adoptive T Cell Therapy. *Cancer Cell*
952 2017;31(5):711-723.e4.

953 5. Böttcher JP et al. NK Cells Stimulate Recruitment of cDC1 into the Tumor
954 Microenvironment Promoting Cancer Immune Control. *Cell* 2018;172(5):1022-
955 1028.e14.

956 6. Chow MT et al. Intratumoral Activity of the CXCR3 Chemokine System Is Required for
957 the Efficacy of Anti-PD-1 Therapy. *Immunity* 2019;50(6):1498-1512.e5.

958 7. Gerhard GM, Bill R, Messemaker M, Klein AM, Pittet MJ. Tumor-infiltrating dendritic
959 cell states are conserved across solid human cancers. *J. Exp. Med.*
960 2021;218(1):e20200264.

961 8. Schenkel JM et al. Conventional type I dendritic cells maintain a reservoir of
962 proliferative tumor-antigen specific TCF-1+ CD8+ T cells in tumor-draining lymph
963 nodes. *Immunity* 2021;54(10):2338-2353.e6.

964 9. Barry KC et al. A natural killer–dendritic cell axis defines checkpoint therapy–
965 responsive tumor microenvironments. *Nat. Med.* 2018;24(8):1178–1191.

966 10. Sánchez-Paulete AR et al. Cancer immunotherapy with immunomodulatory anti-
967 CD137 and anti–PD-1 monoclonal antibodies requires BATF3-dependent dendritic cells.
968 *Cancer Discov.* 2016;6(1):71–79.

969 11. Salmon H et al. Expansion and Activation of CD103+ Dendritic Cell Progenitors at the
970 Tumor Site Enhances Tumor Responses to Therapeutic PD-L1 and BRAF Inhibition.
971 *Immunity* 2016;44(4):924–938.

972 12. Garris CS et al. Successful Anti-PD-1 Cancer Immunotherapy Requires T Cell-
973 Dendritic Cell Crosstalk Involving the Cytokines IFN-γ and IL-12. *Immunity*
974 2018;49(6):1148-1161.e7.

975 13. Hammerich L et al. Systemic clinical tumor regressions and potentiation of PD1
976 blockade with in situ vaccination. *Nat. Med.* 2019;25(5):814–824.

977 14. Oba T et al. Overcoming primary and acquired resistance to anti-PD-L1 therapy by
978 induction and activation of tumor-residing cDC1s. *Nat. Commun.* 2020;11(1).
979 doi:10.1038/s41467-020-19192-z

980 15. Maier B et al. A conserved dendritic-cell regulatory program limits antitumour
981 immunity. *Nature* 2020;580:256–262.

982 16. Di Pilato M et al. CXCR6 positions cytotoxic T cells to receive critical survival signals
983 in the tumor microenvironment. *Cell* 2021;184(17):4512-4530.e22.

984 17. Binnewies M et al. Unleashing Type-2 Dendritic Cells to Drive Article Unleashing
985 Type-2 Dendritic Cells to Drive Protective Antitumor CD4 + T Cell Immunity. *Cell*
986 2019;177:1–16.

987 18. Walter P, Ron D. The unfolded protein response: From stress pathway to
988 homeostatic regulation. *Science (80-.).* 2011;334(6059):1081–1086.

989 19. Yoshida H, Matsui T, Yamamoto A, Okada T, Mori K. XBP1 mRNA Is Induced by ATF6
990 and Spliced by IRE1 in Response to ER Stress to Produce a Highly Active Transcription
991 Factor2001;107:881–891.

992 20. Calfon M et al. IRE1 couples endoplasmic reticulum load to secretory capacity by
993 processing the XBP-1 mRNA2002;415(January):1–6.

994 21. Hollien J et al. Regulated Ire1-dependent decay of messenger RNAs in mammalian
995 cells. *J. Cell Biol.* 2009;186(3):323–331.

996 22. Maurel M, Chevet E, Tavernier J, Gerlo S. Getting RIDD of RNA: IRE1 in cell fate
997 regulation. *Trends Biochem. Sci.* 2014;39(5):245–254.

998 23. Wang JM et al. IRE1 prevents hepatic steatosis by processing and promoting the
999 degradation of select microRNAs. *Sci. Signal.* 2018;11(530):eaao4617.

1000 24. Fink SL et al. IRE1a promotes viral infection by conferring resistance to apoptosis.
1001 *Sci. Signal.* 2017;10(482):eaai7814.

1002 25. Tavernier SJ et al. Regulated IRE1-dependent mRNA decay sets the threshold for
1003 dendritic cell survival. *Nat. Cell Biol.* 2017;19(6):698–710.

1004 26. Osorio F et al. The unfolded-protein-response sensor IRE-1α regulates the function
1005 of CD8α+ dendritic cells. *Nat. Immunol.* 2014;15(3):248–257.

1006 27. Chen X, Cubillos-Ruiz JR. Endoplasmic reticulum stress signals in the tumour and its
1007 microenvironment. *Nat. Rev. Cancer* 2020;21(February):71–88.

1008 28. Song M, Cubillos-ruiz JR. Endoplasmic Reticulum Stress Responses in Intratumoral
1009 Immune Cells : Implications for Cancer Immunotherapy. *Trends Immunol.*
1010 2019;40(2):128–141.

1011 29. Guilliams M et al. Unsupervised High-Dimensional Analysis Aligns Dendritic Cells
1012 across Tissues and Species. *Immunity* 2016;45(3):669–684.

1013 30. Cubillos-Ruiz JR et al. ER Stress Sensor XBP1 Controls Anti-tumor Immunity by
1014 Disrupting Dendritic Cell Homeostasis. *Cell* 2015;161(7):1527–1538.

1015 31. Dong H et al. The IRE1 endoplasmic reticulum stress sensor activates natural killer
1016 cell immunity in part by regulating c-Myc. *Nat. Immunol.* 2019;20(7):865–878.

1017 32. Song M et al. IRE1α–XBP1 controls T cell function in ovarian cancer by regulating
1018 mitochondrial activity. *Nature* 2018;562(7727):423–428.

1019 33. Iwawaki T, Akai R, Kohno K, Miura M. A transgenic mouse model for monitoring
1020 endoplasmic reticulum stress. *Nat. Med.* 2004;10(1):98–102.

1021 34. Mach N et al. Differences in dendritic cells stimulated in vivo by tumors engineered
1022 to secrete granulocyte-macrophage colony-stimulating factor or Flt3-ligand. *Cancer Res.*
1023 2000;60(12):3239–3246.

1024 35. Ruhland MK et al. Visualizing Synaptic Transfer of Tumor Antigens among Dendritic
1025 Cells. *Cancer Cell* 2020;37(6):786-799.e5.

1026 36. Lee A, Scapa E, Cohen D, Glimcher L. Regulation of hepatic lipogenesis by the
1027 transcription factor XBP1. *Science* 2008;320(5882):1492–1496.

1028 37. Caton ML, Smith-Raska MR, Reizis B. Notch–RBP-J signaling controls the homeostasis
1029 of CD8 ⁻ dendritic cells in the spleen. *J. Exp. Med.* 2007;204(7):1653–1664.

1030 38. Cells CCD et al. Notch Signaling Facilitates In Vitro Generation of Resource Notch
1031 Signaling Facilitates In Vitro Generation of Cross-Presenting Classical Dendritic
1032 Cells2018;3658–3672.

1033 39. Balan S et al. Large-Scale Human Dendritic Cell Differentiation Revealing Notch-
1034 Dependent Lineage Bifurcation and Heterogeneity. *Cell Rep.* 2018;24(7):1902-1915.e6.

1035 40. Overwijk WW et al. Tumor Regression and Autoimmunity after Reversal of a
1036 Functionally Tolerant State of Self-reactive CD8 ⁺ T Cells. *J. Exp. Med.* 2003;198(4):569–
1037 580.

1038 41. Miller BC et al. Subsets of exhausted CD8+ T cells differentially mediate tumor
1039 control and respond to checkpoint blockade. *Nat. Immunol.* 2019;20(3):326–336.

1040 42. Philip M, Schietinger A. CD8+ T cell differentiation and dysfunction in cancer. *Nat.*
1041 *Rev. Immunol.* 2021;Online ahead of print.

1042 43. Chen Z et al. TCF-1-Centered Transcriptional Network Drives an Effector versus
1043 Exhausted CD8 T Cell-Fate Decision. *Immunity* 2019;51(5):840-855.e5.

1044 44. Sade-Feldman M et al. Defining T Cell States Associated with Response to Checkpoint
1045 Immunotherapy in Melanoma. *Cell* 2018;175(4):998-1013.e20.

1046 45. Iwawaki T, Akai R, Yamanaka S, Kohno K. Function of IRE1 alpha in the placenta is
1047 essential for placental development and embryonic viability. *Proc. Natl. Acad. Sci. U. S. A.*
1048 2009;106(39):16657–16662.

1049 46. Lee AS. The ER chaperone and signaling regulator GRP78/BiP as a monitor of
1050 endoplasmic reticulum stress. *Methods* 2005;35(4):373–381.

1051 47. So JS et al. Silencing of lipid metabolism genes through ire1α-mediated Mrna decay
1052 lowers plasma lipids in mice. *Cell Metab.* 2012;16(4):487–499.

1053 48. Janssens S, Pulendran B, Lambrecht BN. Emerging functions of the unfolded protein
1054 response in immunity. *Nat. Immunol.* 2014;15(10):910–919.

1055 49. Grootjans J, Kaser A, Kaufman RJ, Blumberg RS. The unfolded protein response in
1056 immunity and inflammation. *Nat. Rev. Immunol.* 2016;16(8):469–484.

1057 50. Shaffer AL et al. XBP1, downstream of Blimp-1, expands the secretory apparatus and
1058 other organelles, and increases protein synthesis in plasma cell differentiation.
1059 *Immunity* 2004;21(1):81–93.

1060 51. Bettigole SE et al. The transcription factor XBP1 is selectively required for eosinophil
1061 differentiation. *Nat. Immunol.* 2015;16(8):829–837.

1062 52. Batista A et al. IRE1α regulates macrophage polarization, PD-L1 expression, and
1063 tumor survival. *PLoS Biol.* 2020;18(6):1–26.

1064 53. Scarlett UK et al. Ovarian cancer progression is controlled by phenotypic changes in
1065 dendritic cells. *J. Exp. Med.* 2012;209(3):495–506.

1066 54. Huarte E et al. Depletion of dendritic cells delays ovarian cancer progression by
1067 boosting antitumor immunity. *Cancer Res.* 2008;68(18):7684–7691.

1068 55. Fuertes MB et al. Host type I IFN signals are required for antitumor CD8 + T cell
1069 responses through CD8α + dendritic cells. *J. Exp. Med.* 2011;208(10):2005–2016.

1070 56. Ferris ST et al. cDC1 prime and are licensed by CD4+ T cells to induce anti-tumour
1071 immunity. *Nature* 2020;584(7822):624–629.

1072 57. Duong E et al. Type I interferon activates MHC class I-dressed CD11b+ conventional
1073 dendritic cells to promote protective anti-tumor CD8+ T cell immunity. *Immunity*
1074 2022;55(2):308-323.e9.

1075 58. MacNabb BW et al. Dendritic cells can prime anti-tumor CD8+ T cell responses
1076 through major histocompatibility complex cross-dressing. *Immunity* 2022;55(6):982-
1077 997.e8.

1078 59. Theisen DJ et al. Batf3-dependent genes control tumor rejection induced by dendritic
1079 cells independently of cross-presentation. *Cancer Immunol. Res.* 2019;7(1):29–39.

1080 60. Marciniak SJ, Chambers JE, Ron D. Pharmacological targeting of endoplasmic
1081 reticulum stress in disease. *Nat. Rev. Drug Discov.* 2022;21(2):115–140.

1082 61. Guttman O et al. Antigen-derived peptides engage the ER stress sensor IRE1α to curb
1083 dendritic cell cross-presentation. *J. Cell Biol.* 2022;221(6). doi:10.1083/jcb.202111068

1084 62. Guo-Ping S et al. Cathepsin S required for normal MHC class II peptide loading and
1085 germinal center development. *Immunity* 1999;10(2):197–206.

1086 63. Finak G, Jiang W, Gottardo R. CytoML for cross-platform cytometry data sharing.
1087 *Cytom. Part A* 2018;93(12):1189–1196.

1088 64. Ellis B et al. flowCore: flowCore: Basic structures for flow cytometry data2021;

1089 65. Finak G, Jiang M. flowWorkspace: Infrastructure for representing and interacting
1090 with gated and ungated cytometry data sets2021;

1091 66. Krijthe JH. Rtsne: T-Distributed Stochastic Neighbor Embedding using a Barnes-Hut
1092 Implementation2015;

1093 67. Hahsler M, Piekenbrock M, Doran D. Dbscan: Fast density-based clustering with R. *J.*
1094 *Stat. Softw.* 2019;91(1). doi:10.18637/jss.v091.i01

1095 68. Wickham H. *ggplot2: Elegant Graphics for Data Analysis*. Springer-Verlag New York;
1096 2016:

1097 69. Ritchie ME et al. Limma powers differential expression analyses for RNA-sequencing
1098 and microarray studies. *Nucleic Acids Res.* 2015;43(7):e47.

1099 70. Robinson M, McCarthy D, Smyth G. edgeR: a Bioconductor package for differential
1100 expression analysis of digital gene expression data. *Bioinformatics* 2010;26:139–140.

1101 71. Kolde R. pheatmap: Pretty Heatmaps2019;

1102 72. Wu T et al. clusterProfiler 4.0: A universal enrichment tool for interpreting omics
1103 data. *Innov.* 2021;2(3):100141.

1104

Figure 1

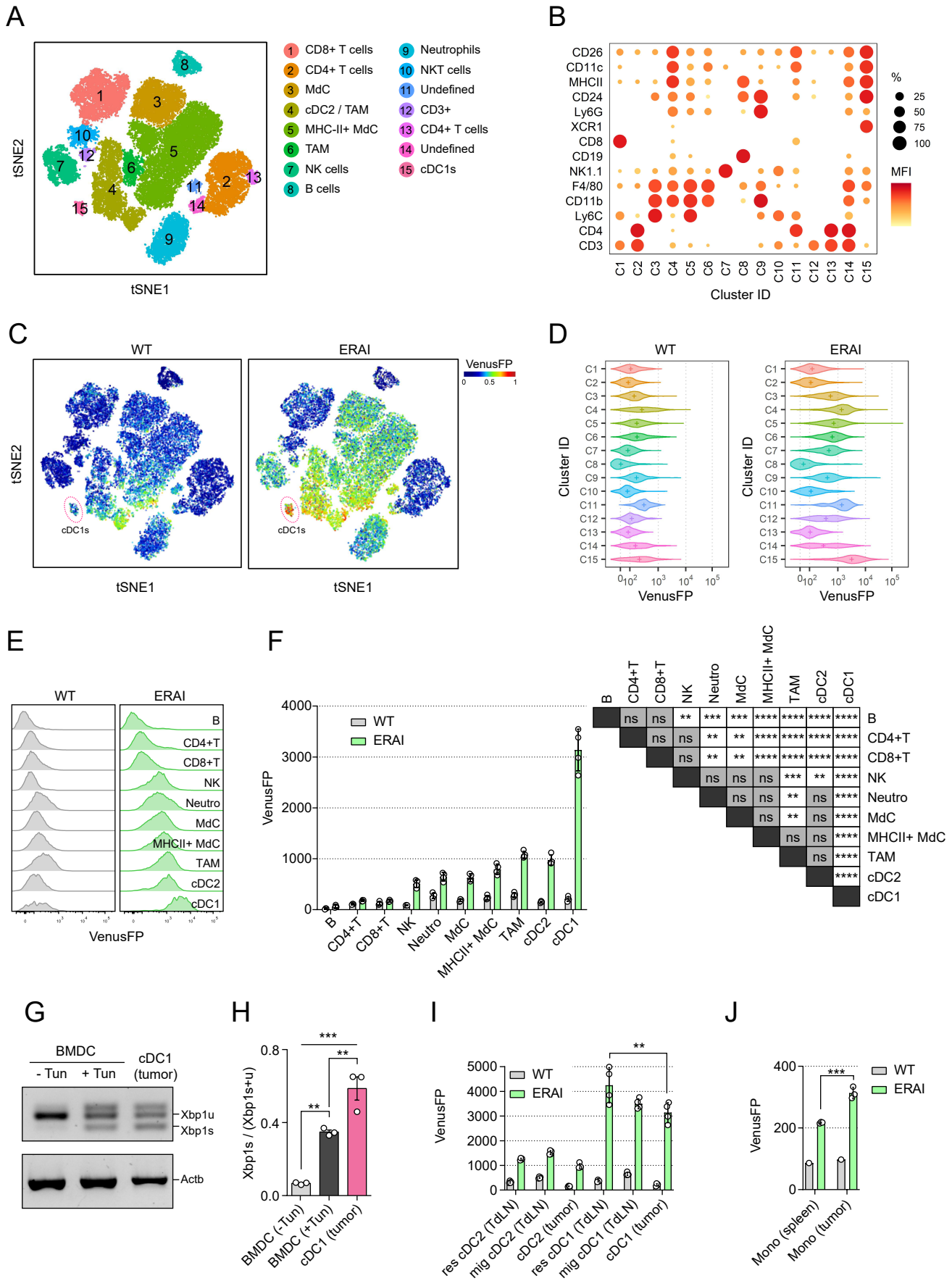
A
tSNE2
tSNE1
1 CD8+ T cells
2 CD4+ T cells
3 MdC
4 cDC2 / TAM
5 MHC-II+ MdC
6 TAM
7 NK cells
8 B cells
9 Neutrophils
10 NKT cells
11 Undefined
12 CD3+
13 CD4+ T cells
14 Undefined
15 cDC1s
B
CD26
CD11c
MHCII
CD24
Ly6G
XCR1
CD8
CD19
NK1.1
F4/80
CD11b
Ly6C
CD4
CD3
Cluster ID
%
25
50
75
100
MFI
C
WT
ERAI
VenusFP
cDC1s
D
Cluster ID
VenusFP
E
WT
ERAI
B
CD4+T
CD8+T
NK
Neutro
MdC
MHCII+ MdC
TAM
cDC2
cDC1
F
WT
ERAI
VenusFP
G
BMDC
- Tun
+ Tun
cDC1 (tumor)
Xbp1u
Xbp1s
Actb
H
Xbp1s / (Xbp1s+u)
BMDC (-Tun)
BMDC (+Tun)
cDC1 (tumor)
I
res cDC2 (TdLN)
mig cDC2 (TdLN)
cDC2 (tumor)
res cDC1 (TdLN)
mig cDC1 (TdLN)
cDC1 (tumor)
J
Mono (spleen)
Mono (tumor)

Figure 2

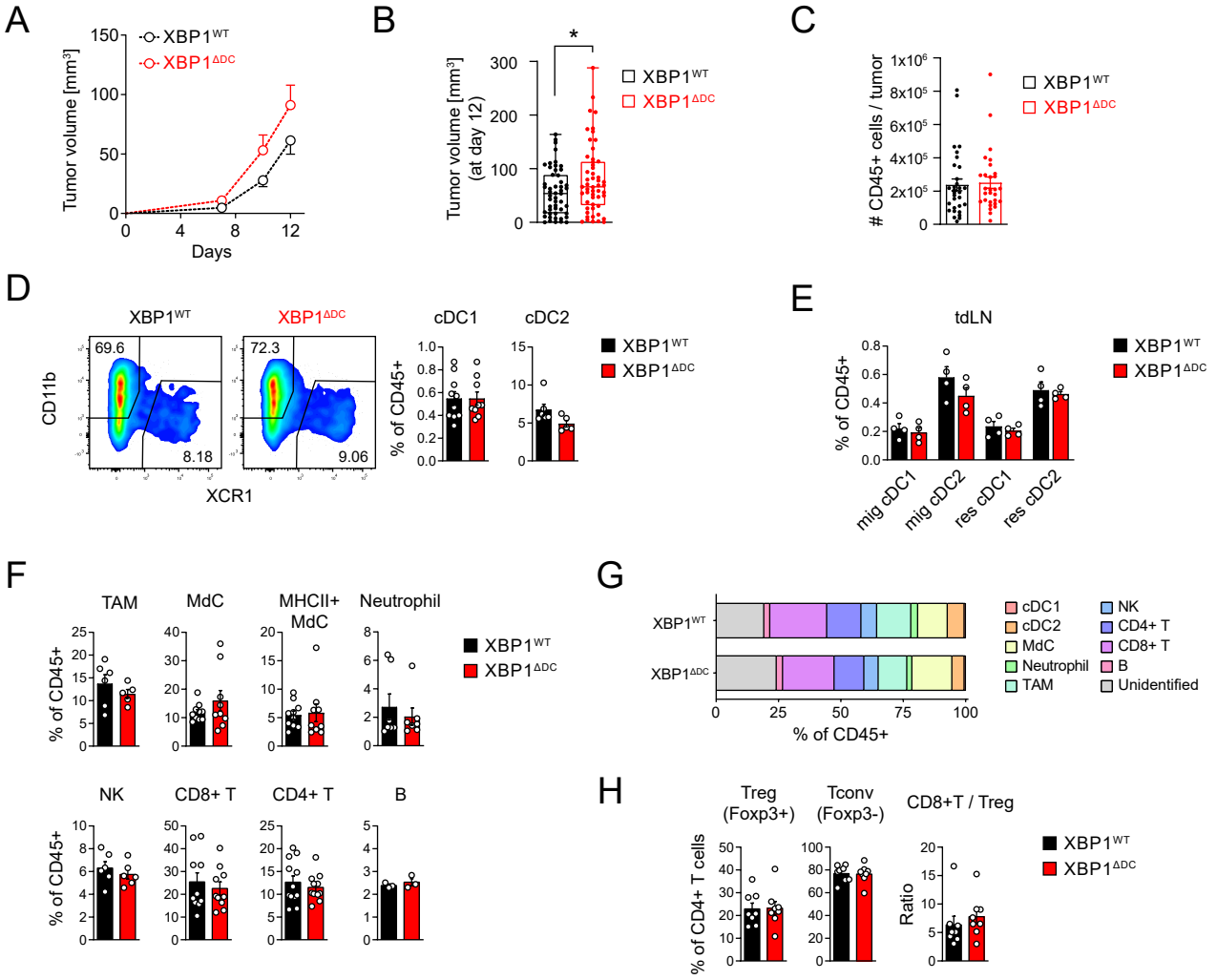
A
XBP1WT
XBP1ΔDC
Tumor volume [mm3]
Days
B
Tumor volume [mm3] (at day 12)
*
C
CD45+ cells / tumor
D
XBP1WT
XBP1ΔDC
CD11b
XCR1
69.6
8.18
72.3
9.06
cDC1
cDC2
% of CD45+
E
tdLN
mig cDC1
mig cDC2
res cDC1
res cDC2
F
TAM
MdC
MHCII+ MdC
Neutrophil
NK
CD8+ T
CD4+ T
B
G
% of CD45+
cDC1
cDC2
MdC
Neutrophil
TAM
NK
CD4+ T
CD8+ T
B
Unidentified
H
Treg (Foxp3+)
Tconv (Foxp3-)
CD8+T / Treg
% of CD4+ T cells
Ratio

Figure 3

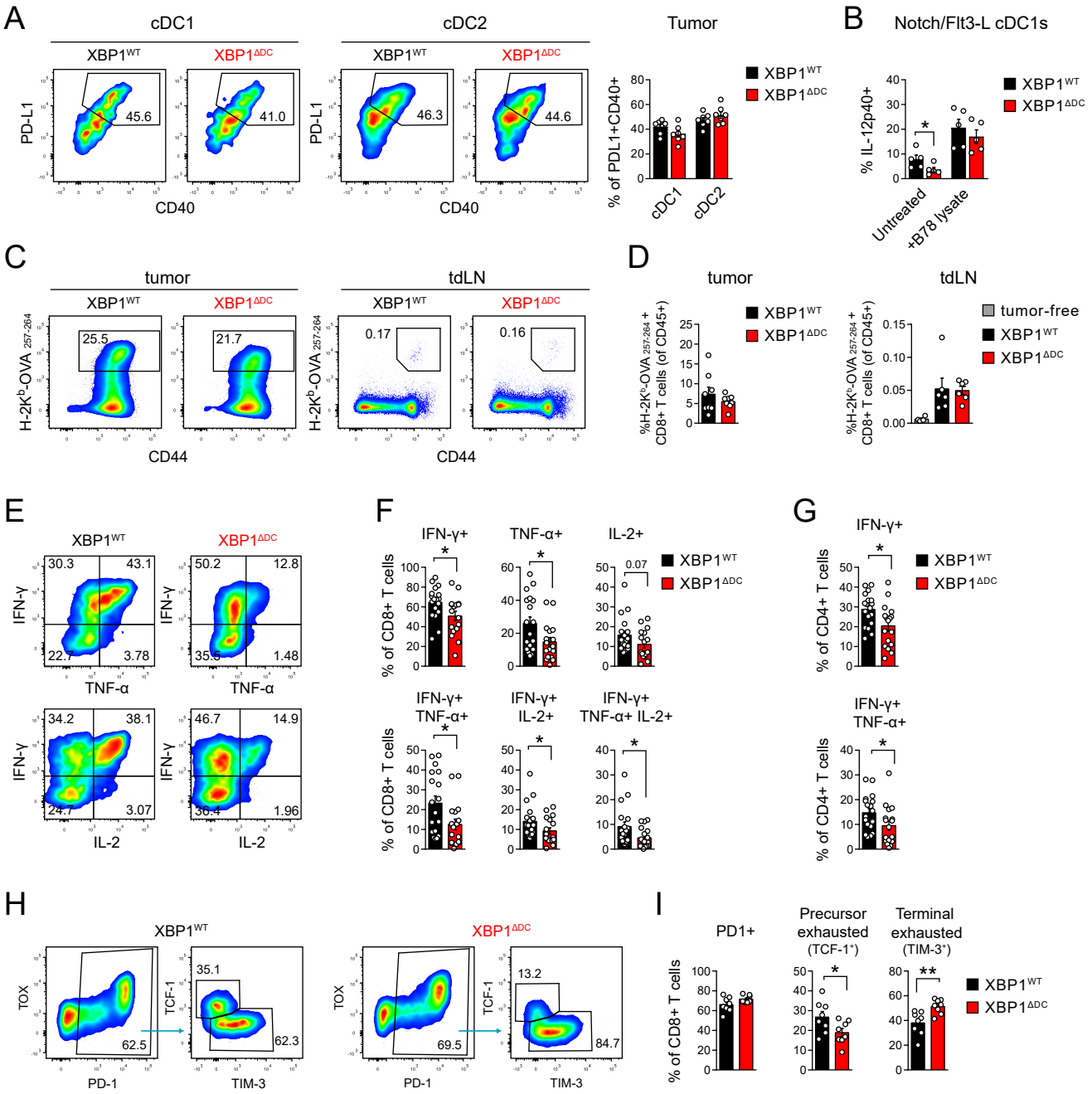
A
cDC1
cDC2
Tumor
XBP1WT
XBP1ΔDC
PD-L1
CD40
45.6
41.0
46.3
44.6
% of PDL1+CD40+
B
Notch/Flt3-L cDC1s
% IL-12p40+
Untreated
+B78 lysate
C
tumor
tdLN
H-2Kb-OVA 257-264
CD44
25.5
21.7
0.17
0.16
D
%H-2Kb-OVA 257-264 + CD8+ T cells (of CD45+)
tumor-free
E
IFN-γ
TNF-α
IL-2
30.3
43.1
22.7
3.78
50.2
12.8
35.5
1.48
34.2
38.1
24.7
3.07
46.7
14.9
36.4
1.96
F
IFN-γ+
TNF-α+
IL-2+
IFN-γ+ TNF-α+
IFN-γ+ IL-2+
IFN-γ+ TNF-α+ IL-2+
% of CD8+ T cells
0.07
G
% of CD4+ T cells
H
TOX
TCF-1
PD-1
TIM-3
62.5
35.1
62.3
69.5
13.2
84.7
I
PD1+
Precursor exhausted (TCF-1+)
Terminal exhausted (TIM-3+)

Figure 4

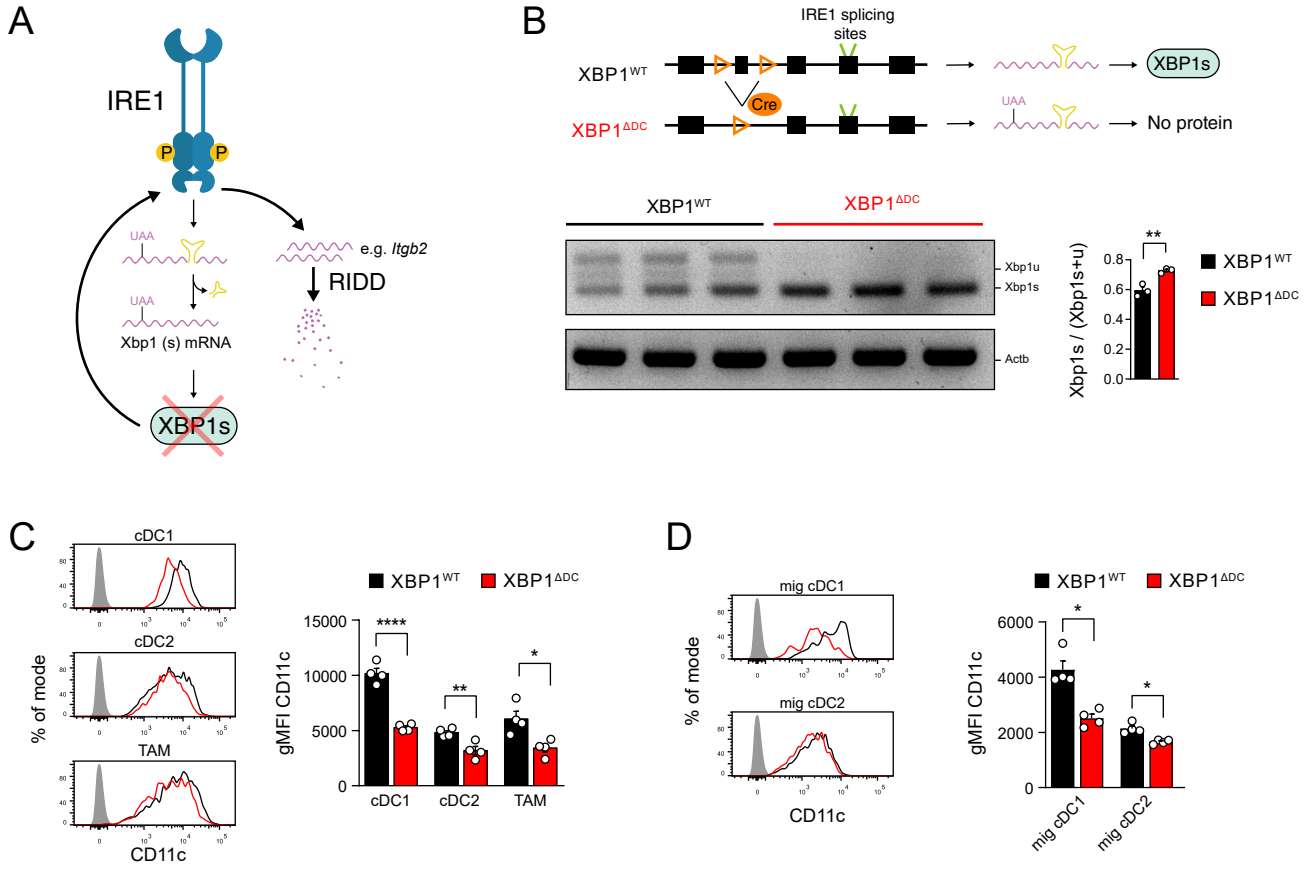
A
IRE1
P
P
UAA
UAA
Xbp1 (s) mRNA
XBP1s
e.g. Itgb2
RIDD
B
IRE1 splicing sites
XBP1WT
Cre
XBP1ΔDC
UAA
XBP1s
No protein
XBP1WT
XBP1ΔDC
Xbp1u
Xbp1s
Actb
Xbp1s / (Xbp1s+u)
0.8
0.6
0.4
0.2
0.0
**
XBP1WT
XBP1ΔDC
C
cDC1
cDC2
TAM
% of mode
CD11c
XBP1WT
XBP1ΔDC
gMFI CD11c
15000
10000
5000
0
****
**
*
cDC1
cDC2
TAM
D
mig cDC1
mig cDC2
% of mode
CD11c
XBP1WT
XBP1ΔDC
gMFI CD11c
6000
4000
2000
0
*
*
mig cDC1
mig cDC2

Figure 5

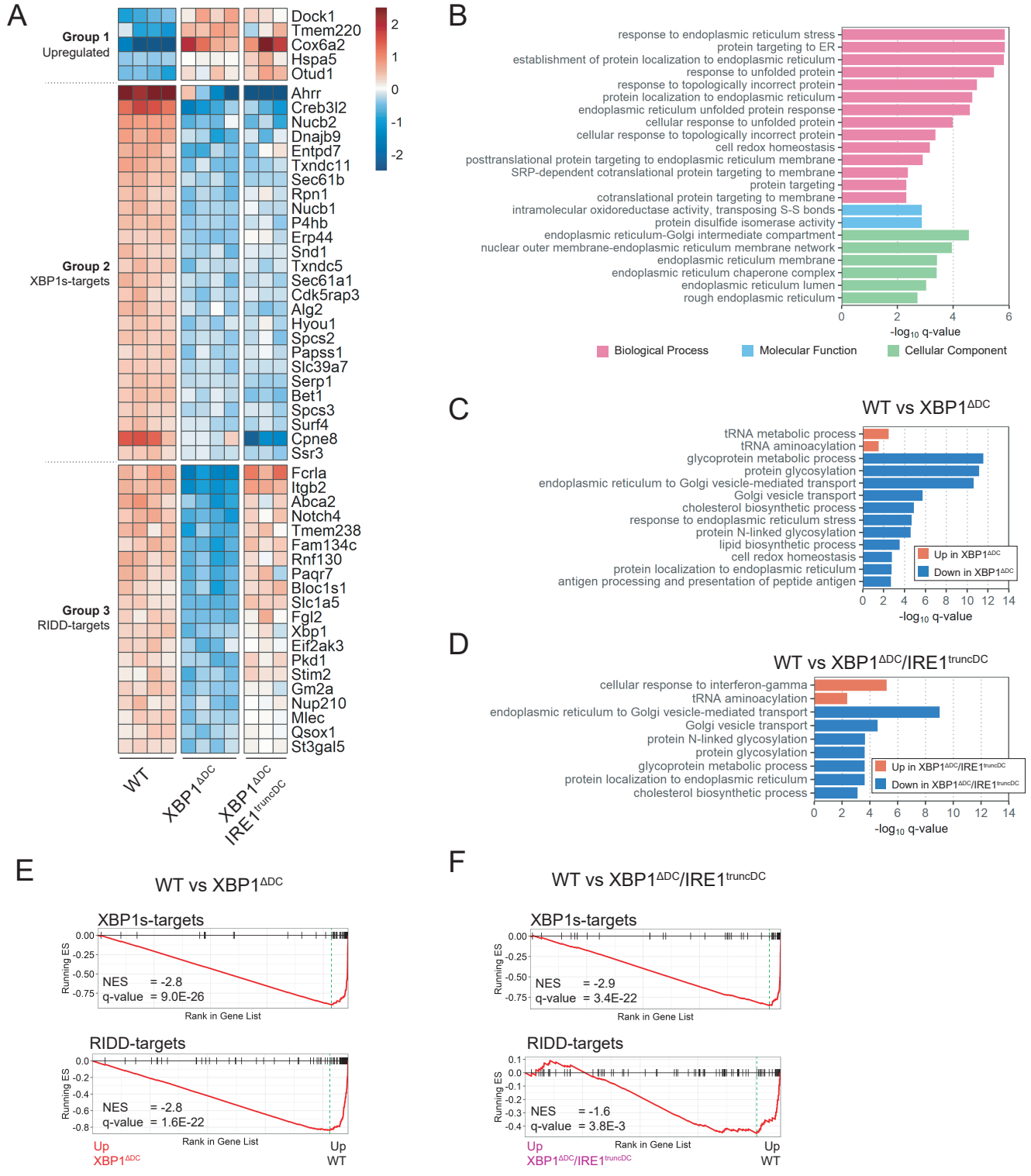
A
Group 1
Upregulated
Dock1
Tmem220
Cox6a2
Hspa5
Otud1
Group 2
XBP1s-targets
Ahrr
Creb3l2
Nucb2
Dnajb9
Entpd7
Txndc11
Sec61b
Rpn1
Nucb1
P4hb
Erp44
Snd1
Txndc5
Sec61a1
Cdk5rap3
Alg2
Hyou1
Spcs2
Papss1
Slc39a7
Serp1
Bet1
Spcs3
Surf4
Cpne8
Ssr3
Group 3
RIDD-targets
Fcrla
Itgb2
Abca2
Notch4
Tmem238
Fam134c
Rnf130
Paqr7
Bloc1s1
Slc1a5
Fgl2
Xbp1
Eif2ak3
Pkd1
Stim2
Gm2a
Nup210
Mlec
Qsox1
St3gal5
2
1
0
-1
-2
WT
XBP1ΔDC
XBP1ΔDC IRE1truncDC
B
response to endoplasmic reticulum stress
protein targeting to ER
establishment of protein localization to endoplasmic reticulum
response to unfolded protein
response to topologically incorrect protein
protein localization to endoplasmic reticulum
endoplasmic reticulum unfolded protein response
cellular response to unfolded protein
cellular response to topologically incorrect protein
cell redox homeostasis
posttranslational protein targeting to endoplasmic reticulum membrane
SRP-dependent cotranslational protein targeting to membrane
protein targeting
cotranslational protein targeting to membrane
intramolecular oxidoreductase activity, transposing S-S bonds
protein disulfide isomerase activity
endoplasmic reticulum-Golgi intermediate compartment
nuclear outer membrane-endoplasmic reticulum membrane network
endoplasmic reticulum membrane
endoplasmic reticulum chaperone complex
endoplasmic reticulum lumen
rough endoplasmic reticulum
0
2
4
6
-log10 q-value
Biological Process
Molecular Function
Cellular Component
C
WT vs XBP1ΔDC
tRNA metabolic process
tRNA aminoacylation
glycoprotein metabolic process
protein glycosylation
endoplasmic reticulum to Golgi vesicle-mediated transport
Golgi vesicle transport
cholesterol biosynthetic process
response to endoplasmic reticulum stress
protein N-linked glycosylation
lipid biosynthetic process
cell redox homeostasis
protein localization to endoplasmic reticulum
antigen processing and presentation of peptide antigen
Up in XBP1ΔDC
Down in XBP1ΔDC
0 2 4 6 8 10 12 14
-log10 q-value
D
WT vs XBP1ΔDC/IRE1truncDC
cellular response to interferon-gamma
tRNA aminoacylation
endoplasmic reticulum to Golgi vesicle-mediated transport
Golgi vesicle transport
protein N-linked glycosylation
protein glycosylation
glycoprotein metabolic process
protein localization to endoplasmic reticulum
cholesterol biosynthetic process
Up in XBP1ΔDC/IRE1truncDC
Down in XBP1ΔDC/IRE1truncDC
0 2 4 6 8 10 12 14
-log10 q-value
E
WT vs XBP1ΔDC
XBP1s-targets
Running ES
0.00
-0.25
-0.50
-0.75
NES = -2.8
q-value = 9.0E-26
Rank in Gene List
RIDD-targets
0.0
-0.2
-0.4
-0.6
-0.8
NES = -2.8
q-value = 1.6E-22
Up XBP1ΔDC
Rank in Gene List
Up WT
F
WT vs XBP1ΔDC/IRE1truncDC
XBP1s-targets
Running ES
0.00
-0.25
-0.50
-0.75
NES = -2.9
q-value = 3.4E-22
Rank in Gene List
RIDD-targets
0.1
0.0
-0.1
-0.2
-0.3
-0.4
NES = -1.6
q-value = 3.8E-3
Up XBP1ΔDC/IRE1truncDC
Rank in Gene List
Up WT

Figure 6

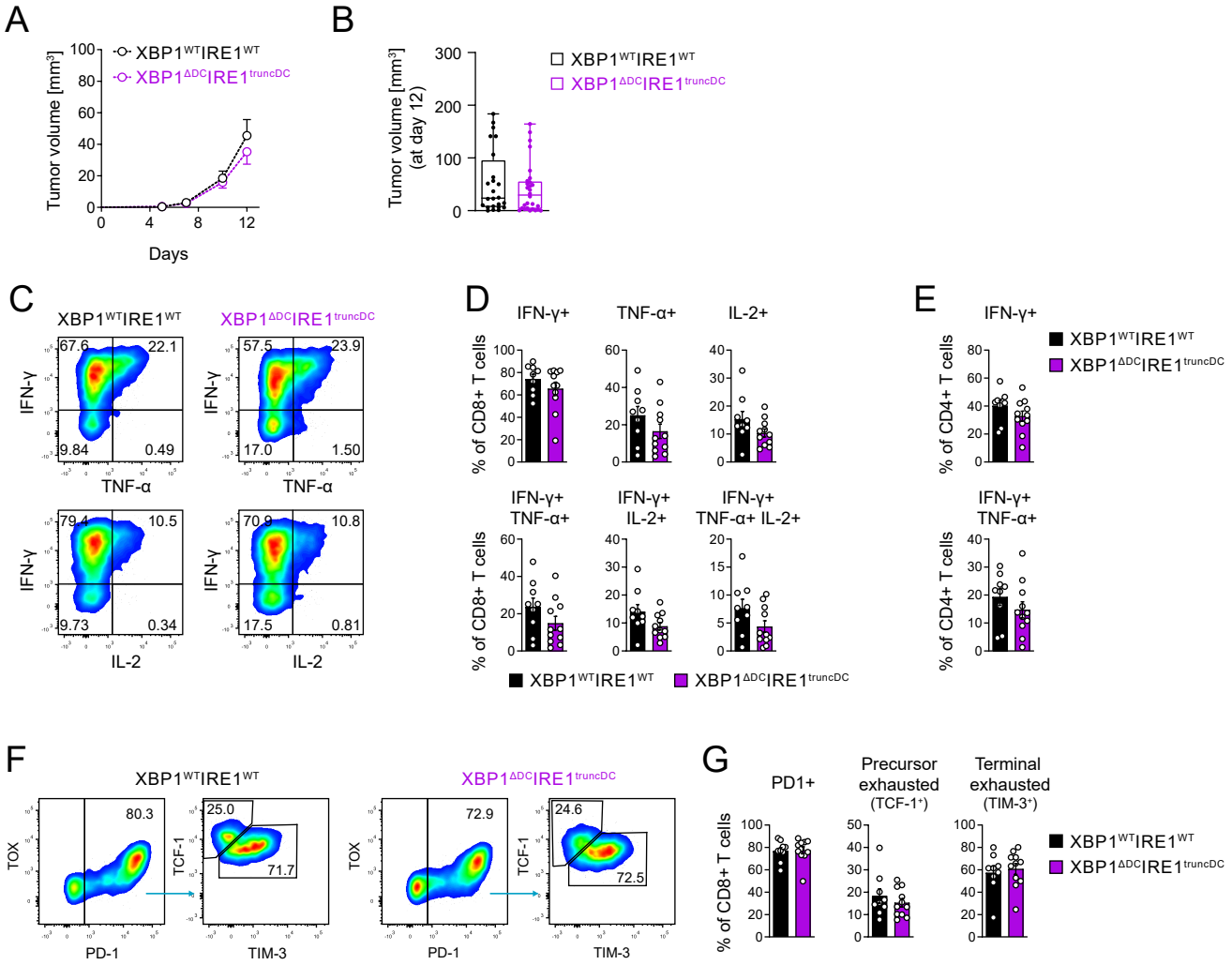
A
Tumor volume [mm³]
XBP1WTIRE1WT
XBP1ΔDCIRE1truncDC
Days
B
Tumor volume [mm³] (at day 12)
C
IFN-γ
TNF-α
IL-2
67.6
22.1
9.84
0.49
57.5
23.9
17.0
1.50
79.4
10.5
9.73
0.34
70.9
10.8
17.5
0.81
D
IFN-γ+
TNF-α+
IL-2+
IFN-γ+ TNF-α+
IFN-γ+ IL-2+
IFN-γ+ TNF-α+ IL-2+
% of CD8+ T cells
E
% of CD4+ T cells
F
TOX
TCF-1
PD-1
TIM-3
80.3
25.0
71.7
72.9
24.6
72.5
G
PD1+
Precursor exhausted (TCF-1+)
Terminal exhausted (TIM-3+)